

2

AFGL-TR-84-0317

ENVIRONMENTAL RESEARCH PAPERS, NO. 902

AD-A157 080

Precipitating Electron and Ion Detectors (SSJ/4)  
for the Block 5D/Flights 6-10 DMSP Satellites:  
Calibration and Data Presentation

D. A. HARDY  
L. K. SCHMITT, 1Lt, USAF  
M. S. GUSSENHOVEN  
F. J. MARSHALL

H. C. YEH  
T. L. SCHUMAKER  
A. HUBER  
J. PANTAZIS



21 November 1984

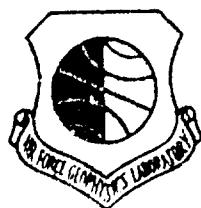


Approved for public release; distribution unlimited.



DTIC  
ELECTE  
JUL 26 1985  
S B D

DTIC FILE COPY



SPACE PHYSICS DIVISION

PROJECT 7601

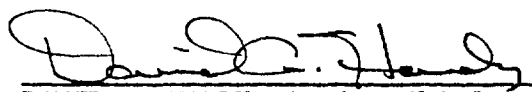
**AIR FORCE GEOPHYSICS LABORATORY**

HANSCOM AFB, MA 01731

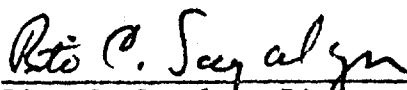
85 07 15 313

"This technical report has been reviewed and is approved for publication"

FOR THE COMMANDER



DAVID A. HARDY, Acting Chief  
Space Particles Environment Branch  
Space Physics Division



Rita C. Sagalyn, Director  
Space Physics Division

This report has been reviewed by the ESD Public Affairs Office (PA) and is releasable to the National Technical Information Services (NTIS).

Qualified requestors may obtain additional copies from the Defense Technical Information Center. All others should apply to the National Technical Information Service.

If your address has changed, or if you wish to be removed from the mailing list, or if the addressee is no longer employed by your organization, please notify AFGL/DAA, Hanscom AFB, MA 01731. This will assist us in maintaining a current mailing list.

Unclassified

SECURITY CLASSIFICATION OF THIS PAGE

REPORT DOCUMENTATION PAGE				
1a. REPORT SECURITY CLASSIFICATION Unclassified			1b. RESTRICTIVE MARKINGS	
2a. SECURITY CLASSIFICATION AUTHORITY			3. DISTRIBUTION/AVAILABILITY OF REPORT Approved for public release; distribution unlimited.	
2b. DECLASSIFICATION/DOWNGRADING SCHEDULE				
4. PERFORMING ORGANIZATION REPORT NUMBER(S) AFGL-TR-84-0317 ERP, No. 902			5. MONITORING ORGANIZATION REPORT NUMBER(S)	
6a. NAME OF PERFORMING ORGANIZATION Air Force Geophysics Laboratory		6b. OFFICE SYMBOL (If applicable) PHP		7a. NAME OF MONITORING ORGANIZATION
6c. ADDRESS (City, State and ZIP Code) Hanscom AFB Massachusetts 01731			7b. ADDRESS (City, State and ZIP Code) Hanscom AFB Massachusetts 01731	
8a. NAME OF FUNDING/SPONSORING ORGANIZATION		8b. OFFICE SYMBOL (If applicable)		9. PROCUREMENT INSTRUMENT IDENTIFICATION NUMBER
8c. ADDRESS (City, State and ZIP Code)			10. SOURCE OF FUNDING NOS.	
			PROGRAM ELEMENT NO. 62101	PROJECT NO. 7601
			TASK NO. 20	WORK UNIT NO. 01
11. TITLE (Include Security Classification) Precipitating Electron & Ion (Contd)				
12. PERSONAL AUTHOR(S) D. A. Hardy, L. K. Schmitt, 1Lt, USAF, M. S. Gussenhoven, F. J. Marshall, H. C. Yeh*, T. L. Schumaker*, A. Huber**, and J. Pantazis**				
13a. TYPE OF REPORT In-House Scientific		13b. TIME COVERED FROM _____ TO _____		14. DATE OF REPORT (Yr., Mo., Day) 1984 November 21
15. PAGE COUNT 60				
16. SUPPLEMENTARY NOTATION * Boston College, Chestnut Hill, Massachusetts 02167 ** Emmanuel College, Lexington, Massachusetts 02173				
17. COSATI CODES			18. SUBJECT TERMS (Continue on reverse if necessary and identify by block number)	
FIELD	GROUP	SUB. GR.	Aurora	
			Defense meteorological satellite program (DMSP)	
			Precipitating ions & electrons	
19. ABSTRACT (Continue on reverse if necessary and identify by block number) The satellites of the Defense Meteorological Satellite Program (DMSP) are flown operationally to provide data for the specification of terrestrial weather and the near earth space environment. In support of space environment specification the satellites starting with F6, carry an improved set of electrostatic analyzers SSJ/4, designed to measure the flux of precipitating electrons and ions with energies between 30 eV and 30 keV. The data from these analyzers are routinely processed at AFGL and are available to the scientific community. Both by itself, and in combination with other sensors on the satellite, the SSJ/4 detectors provide important data for the study of auroral processes. This report was prepared to facilitate the widespread use of the SSJ/4 data.				
20. DISTRIBUTION/AVAILABILITY OF ABSTRACT UNCLASSIFIED/UNLIMITED <input type="checkbox"/> SAME AS RPT. <input checked="" type="checkbox"/> DTIC USERS <input type="checkbox"/>			21. ABSTRACT SECURITY CLASSIFICATION Unclassified	
22a. NAME OF RESPONSIBLE INDIVIDUAL D. A. Hardy			22b. TELEPHONE NUMBER (Include Area Code) (617) 861-3211	22c. OFFICE SYMBOL PHP

DD FORM 1473, 83 APR

EDITION OF 1 JAN 73 IS OBSOLETE.

Unclassified  
SECURITY CLASSIFICATION OF THIS PAGE

Unclassified

SECURITY CLASSIFICATION OF THIS PAGE(When Data Entered)

11. (Contd)

Detectors (SSJ/4) for the Block 5D/Flights 6-10 DMSP Satellites:  
Calibration and Data Presentation

Unclassified

SECURITY CLASSIFICATION OF THIS PAGE(When Data Entered)

## Preface

The authors acknowledge support for this effort from the Air Force Systems Command, the Air Force Office of Scientific Research, and the Southeastern Center for Electrical Engineering Education (SCEEE). Support for the work of H. C. Yeh and T. L. Schumaker was provided for under AFGL contracts F19628-82-K-0011 and F19628-81-K-0032. Support for the work of F. J. Marshall was provided for under AFGL contract F19628-83-C-0035, and the work of A. Huber and J. Pantazis was provided for under AFGL contract F19628-82-K-0039.

We thank Dennis Dillon for his assistance in preparation of the manuscript and Jack Collins for drafting the figures.

**DTIC**  
**ELECTE**  
**S** **D**  
JUL 26 1985  
**B**

iii

Accession For	
NTIS GRA&I	<input checked="checked" type="checkbox"/>
DTIC TAB	<input type="checkbox"/>
Unannounced	<input type="checkbox"/>
Justification	
By	
Distribution/	
Availability Codes	
Dist	Avail and/or Special
A-1	



## Contents

1. INTRODUCTION	1
2. THE DMSP F6 AND F7 ORBITS	4
3. DESCRIPTION OF THE SSJ/4 DETECTORS	6
4. ELECTRON DETECTORS: CALIBRATION RESULTS AND DERIVED GEOMETRIC FACTORS	7
5. ION DETECTORS: DERIVED GEOMETRIC FACTORS AND CORRECTIONS FOR ELECTRON FLUXES	21
5.1 Derived Ion Geometric Factors	21
5.2 Corrections for Electron Fluxes	22
6. USES OF THE SSJ/4 DATA	26
6.1 Survey Plots	28
6.2 Auroral Electron and Ion Boundaries	31
6.3 Discrete Arcs and Use of Electron Rejection Curves	32
6.4 Ion Signatures in the Polar Rain	42
REFERENCES	45
APPENDIX A: Anomalies in the F6 Electron Detector	47

## Illustrations

1. DMSP Image for 10 January 1983 Gridded in Geographic Coordinates Projected to 110 km	2
2. Combined North Pole Orbital Coverage for DMSP F6 and F7 Plotted in a Corrected Geomagnetic Latitude/Magnetic Local Time Coordinate System	5
3. Combined South Pole Orbital Coverage for DMSP F6 and F7 Plotted in a Corrected Geomagnetic Latitude/Magnetic Local Time Coordinate System	5
4. Photograph of One Sensor Head of the SSJ/4 Electrostatic Analyzer	7
5. The Energy Dependent Geometric Factor, $G(E)$ , Plotted as a Function of Energy for Channel 1 for Detectors F6 (Rice), F8, and F10 (AFGL)	9
6. The Energy Dependent Geometric Factor, $G(E)$ , Plotted as a Function of Energy for Channel 6 for Detectors F6 (Rice), F6 (SWRI), and F10 (AFGL)	10
7. The Energy Dependent Geometric Factor, $G(E)$ , Plotted as a Function of Energy for Channel 11 for Detectors F6 (Rice), F8, and F10 (AFGL)	11
8. The Normalized Energy Dependent Geometric Factor, $G(E)$ Plotted as a Function of the Normalized Energy for Channels 1, 6, and 10 of Detector F6	12
9. The Normalized Energy Dependent Geometric Factor, $G(E)$ , Plotted as a Function of the Normalized Energy for Channels 1, 2, 4, 6, 8, and 10 of Detector F10	13
10. The Normalized Energy Dependent Geometric Factor, $G(E)$ Plotted as a Function of the Normalized Energy for Channels 11, 14, 17, 18, 19, and 20 of Detector F10, Channel 11 of Detector F8, and Channel 11 of Detector F6	14
11. Details of the Configuration of the Apertures and Curved Plates of the Analyzer Showing the Angles $\alpha$ and $\beta$	15
12. Angular Response of Electron Channels 10 and 11 for the SSJ/4 Detectors for the F6, 8, and 10 Satellites	16
13. The Logarithm of the Energy Dependent Geometric Factor, $G(E)$ , of the 6 Calibrated Channels of the Low Energy Electron Analyzer for the F10 Satellite Plotted vs the Logarithm of Energy	16
14. The Logarithm of the Energy Dependent Geometric Factor, $G(E)$ , of the Calibrated Channels of the High Energy Electron Analyzer for the F10 Satellite Plotted vs the Logarithm of Energy	17
15. The Logarithm of the Energy Independent Geometric Factor, $G$ , for the Calibrated Channels of the Low Energy Electron Analyzers for the F8 and F10 Satellites Plotted vs the Logarithm of the Energy	18
16. The Logarithm of the Energy Dependent Geometric Factor for Four of the Low Energy Channels of the Ion Analyzer to Electrons for the F10 Satellite Plotted vs the Logarithm of the Energy	24
17. The Logarithm of the Maximum and Minimum Energy Dependent Geometric Factors for the High Energy Channels of the Ion Analyzers to Electrons for the F10 Satellite Plotted vs the Logarithm of the Energy	25

## Illustrations

18a.	Electron Data From a Northern Hemisphere Pass of the F6 Satellite Occurring Between 15:32 UT (55,920 sec) and 15:57 UT (57,420 sec) on 10 January 1983	29
18b.	Ion Data From a Northern Hemisphere Pass of the F6 Satellite Occurring Between 15:32 UT (55,920 sec) and 15:57 UT (57,420 sec) on 10 January 1983	30
19.	The Logarithm of the Integral Number Flux of Electrons Above 1 keV and 5 keV and the Logarithm of the Inferred Field Aligned Potential All Plotted for the Time Period Between 56,195 and 56,290 sec UT for a Pass of the F6 Satellite on 10 January 1983	34
20.	The Differential Number Flux Spectra for Electrons and Ions at 56,241 sec UT on 10 January 1983	35
21.	The Differential Number Flux Spectra for Electrons and Ions at 56,198 sec UT on 10 January 1983	37
22a.	Electron Data Plotted as in Figure 18 for a North Pole Pass of the F6 Satellite Between 15:02 UT (54,120 sec) and 15:27 UT (55,620 sec) on 21 January 1983	38
22b.	Ion Data Plotted as in Figure 18 for a North Pole Pass of the F6 Satellite Between 15:02 UT (54,120 sec) and 15:27 UT (55,620 sec) on 21 January 1983	39
23.	The Differential Number Flux Spectra for Electrons and Ions at 54,938 sec UT on 21 January 1983	40
24.	The Differential Number Flux Spectra for Electrons and Ions at 54,919 sec UT on 21 January 1983	41
25.	The Logarithm of the Measured Ion Distribution Function in the Polar Rain Plotted vs Energy on a Linear Scale	44
A1.	The Average Ratio of the Counts in Electron Channel 10 to the Counts in Electron Channel 11 Plotted vs the Logarithm of the Average Counts in Electron Channel 10	48
A2.	The Ratio of the True Counts to the Measured Counts for the Low Energy Electron Channels of the F6 SSJ/4 Detector Plotted vs the Logarithm of the Measured Counts	50



## Tables

1. $\Delta\alpha$ and $\Delta\beta$ for F6, F8, and F10, Channels 10 and 11	15
2. Derived Electron Geometric Factors for F8 and F10	19
3. Derived Electron Geometric Factors for F6 and F7	20
4. Derived Ion Geometric Factors for F6 and F7	23
5. Rejection Curve Values	27
6. Electron and Ion Boundaries for 10 January 1983 near 15 UT	32
7. Measured and Corrected Ion Counts for Spectra on 10 and 21 January 1983	36
8. Ion Count Rates for 10 January 1983; an Example of a Maxwellian Distribution	43

## Precipitating Electron and Ion Detectors (SSJ/4) for the Block 5D/Flights 6-10 DMSP Satellites: Calibration and Data Presentation

### 1. INTRODUCTION

The Defense Meteorological Satellite Program (DMSP) of the U. S. Air Force is an operational program calling for two satellites to be in polar orbit at all times: one in the dawn-dusk meridian and one in the 1030 to 2230 meridian. Depending on launch dates and system lifetimes there can be as many as three or as few as one satellite in operation at a given time. The Program is principally devoted to weather monitoring but radiometers operating over darkened areas produce the now familiar images of the auroral regions. These provided the first extended views of auroral phenomena, and are available from 1971 to the present.

Figure 1 is one such DMSP auroral image taken over the northern polar cap on 10 January 1983, from ~15:30 to 15:50 UT. Most of the nightside-half of the instantaneous auroral oval is imaged. The grid is in geographic latitude and longitude. Local midnight is at the left of the image, local dawn is to the center-bottom, and local dusk, center-top. The vertical line across the center of the image is the satellite track. City lights in eastern Russia lie underneath the dusk oval (burning oil fields can be seen in the upper left-hand corner). The diffuse aurora, lying at the equatorward edge of the oval, is evident in the local times sampled. Discrete arcs lie at the poleward edge with two distinct westward traveling surges post-midnight. Understanding the dynamical processes responsible for the immense

---

(Received for publication 20 November 1984)

energy deposition into the earth's upper atmosphere by auroral events such as this occupies a central place in space physics.



Figure 1. DMSP Image for  
10 January 1983 Gridded in  
Geographic Coordinates  
Projected to 110 km

Since 1974, low energy electron analyzers have been placed on satellites in the DMSP program. The satellites are non-spinning and the detectors are positioned to measure precipitating electrons which are responsible for the most intense auroral features. The original electrostatic analyzers measured electrons in six channels from 0.2 to 20 keV. In July 1977, with the launch of DMSP-F2, these were replaced by the SSJ/3 detector, a set of two electrostatic analyzers covering the range 50 eV to 20 keV in 16 energy channels. The SSJ/3 sensors were also flown on the F4 satellite.<sup>1</sup> With DMSP F6, F7, F8 and F10 additional

1. Hardy, D.A., Gussenhoven, M.S., and Huber, A. (1979) The Precipitating Electron Detectors (SSJ/3) for the Block 5D/Flights 2-5 DMSP Satellites: Calibration and Data Presentation, AFGL-TR-79-0210, AD A083136.

electrostatic analyzers have been added to measure the flux of precipitating ions. In addition, the energy range has been extended to 30 eV on the low end and to 30 keV on the high end. Together with the imaging devices, the improved measurements of precipitating electrons and ions will continue to give DMSP a central place in the continuing understanding of auroral and polar cap phenomena, and their relation to magnetospheric dynamics.

The consistently high quality of the precipitating electron measurements on the F2 and F4 satellites led to several very large statistical studies which specify average global auroral properties. The variation of the equatorward boundary (the lowest latitude of diffuse auroral occurrence) was found to be so regular with existing magnetic activity indices<sup>2,3,4</sup> that by accounting for the auroral oval offset in local time the boundary can be used, in turn, to specify auroral activity. An algorithm to automatically select the equatorward boundary<sup>5</sup> from the SSJ/4 electron data is now used by Global Weather Central of the U.S. Air Force to produce a real time measure of auroral activity. Global maps of electron precipitation have been prepared as functions of the KP magnetic index to show variations in integral flux and average energy.<sup>6</sup> Not only are these useful for verification of large-scale simulations of magnetospheric dynamics, but they also provide important information on ionospheric-magnetospheric coupling. The global maps have been used as input to codes that specify both height-integrated and height-varying Hall and Pedersen conductivities as functions of local time, season, and magnetic activity. Finally, the electron data were used to distinguish two very different states of the polar cap: one which is characterized by polar rain, or very weak fluxes of cool electrons; and one characterized by polar showers, or structured, high level fluxes of cool electrons throughout the cap. The first occurs for high auroral oval activity; the second for magnetically quiet times. Statistical maps of polar rain variations across the cap<sup>7</sup> reflect the nearly impossible-to-measure variations in the vast tail lobe regions to which the caps map magnetically. Further, the occurrence and distribution of polar showers<sup>8,9</sup> are central to understanding the occurrence of polar cap auroral activity.<sup>10,11,12,13</sup> It is anticipated that many of these studies will be extended using data from the new precipitating particle sensors and that specifically, the average properties of ion precipitation will be as well specified as the electron precipitation.

Additional instruments on the DMSP satellites which contribute to magnetospheric studies are: The Air Force Geophysics Laboratory SSIE instrument<sup>14</sup> on F6, F7, measuring the ionospheric thermal plasma; SSIES on F8, an extension of SSIE, to include measurements of ion drifts and variations in the thermal density;

---

Due to the large number of references cited above, they will not be listed here. See References, page 45.

a scientific quality magnetometer on F7 provided jointly by the Air Force Geophysics Laboratory and the Applied Physics Laboratory; an X-ray imager on F6 provided by the Aerospace Corporation; and a dosimeter on F7 provided by the Air Force Geophysics Laboratory.

In this report we give sufficient information for the accurate use of the SSJ/4 data. This includes orbital parameters, a description of the instruments, results of the extensive calibration of the instruments, examples of data use, and finally, a précis of the anomalies found in the F6 electron detector. At the time of writing only DMSP satellites F6 and F7 have been launched and SSJ/4 from these satellites analyzed.

## **2. THE DMSP F6 and F7 ORBITS**

The DMSP F6 satellite was launched in December 1982, into a 840-km circular polar orbit, sun-synchronous in the dawn-dusk meridian plane. The DMSP F7 satellite was launched into a similar orbit in the 1030 to 2230 meridian in November 1983. Both satellites have orbital periods of approximately 101 minutes.

Although both satellites are in sun-synchronous orbits, their spatial coverage in magnetic local time (MLT) and geomagnetic latitude (MLAT) is wide due to the diurnal rotation of the geomagnetic pole about the geographic pole. Figures 2 and 3 show the spatial coverage for the two satellites for the north and south poles, respectively. For these figures the orbital positions of the satellites over one day were projected down the field lines to an altitude of 110 km using a Jensen Cain model and the envelope of the projections determined. There is a wide region of spatial overlap in the orbital coverage of the two satellites (cross hatched regions in Figures 2 and 3). Data in these regions can be used for in-flight cross-calibration of the sensors on the two satellites.

If the coverage of the satellites is combined, and both poles used, almost complete coverage of the auroral regions ( $> 60^\circ$  MLAT) is obtained for all local times. Coverage is most limited at latitudes below 70 degrees in the post-midnight sector and below 65 degrees in the post-noon sector. At latitudes corresponding to the polar cap ( $> 75^\circ$  MLAT) the combined coverage is complete for all local times. South pole coverage is principally on the dayside and pre-midnight; while north pole coverage is principally on the nightside and pre-noon.

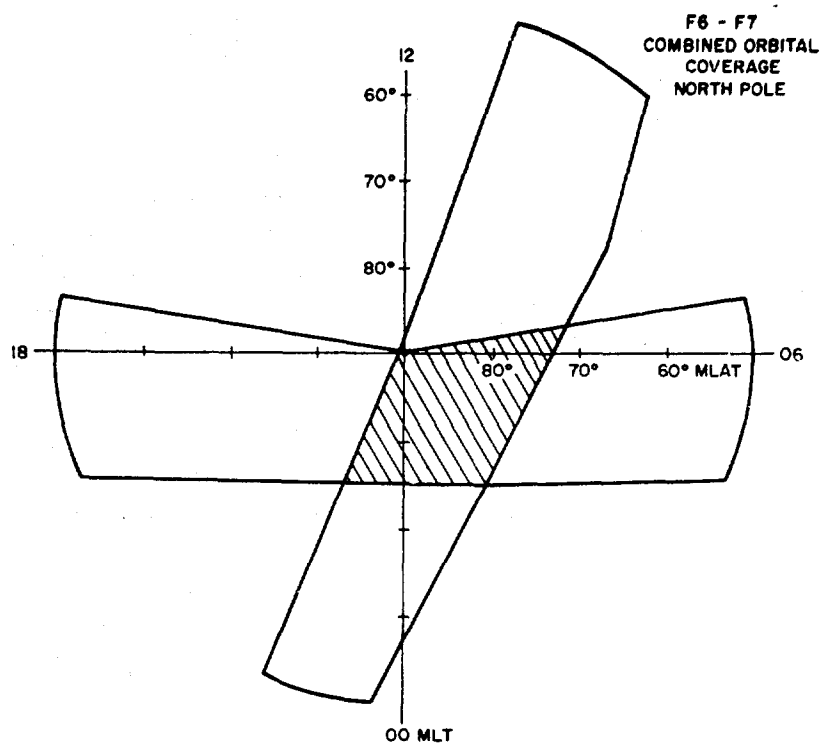


Figure 2. Combined North Pole Orbital Coverage for DMSP F6 and F7 Plotted in a Corrected Geomagnetic Latitude/Magnetic Local Time Coordinate System

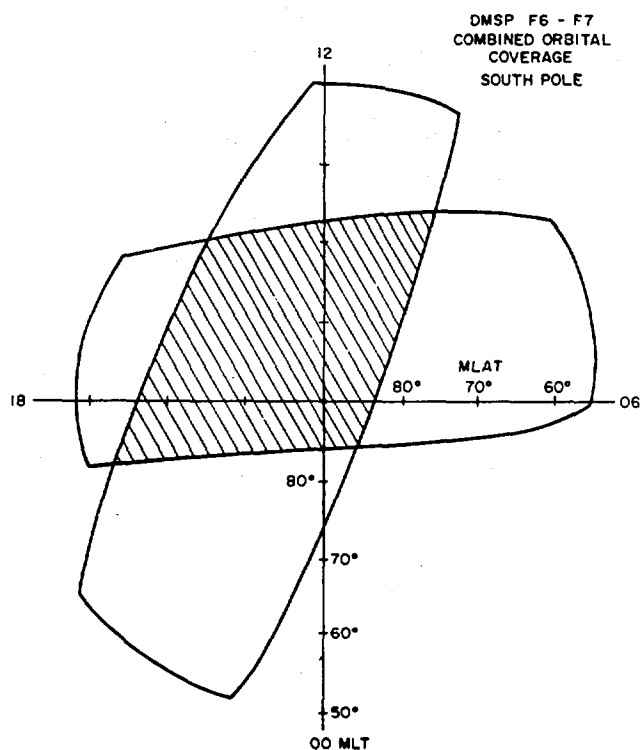


Figure 3. Combined South Pole Orbital Coverage for DMSP F6 and F7 Plotted in a Corrected Geomagnetic Latitude/Magnetic Local Time Coordinate System

### 3. DESCRIPTION OF THE SSJ/4 DETECTORS

The SSJ/4 sensors flown on the F6, F7, F8, and F10 satellites are identical in design. They measure the flux of electrons and ions in 20 energy channels in the range from 30 to 30,000 eV. This is accomplished using a set of four cylindrical curved plate electrostatic analyzers arranged in two pairs. Each analyzer consists of three basic components; an aperturing system, a set of two concentric cylindrical curved plates, and a pair of channeltrons. A photograph of one pair of analyzers is shown in Figure 4. The aperture system collimates the incoming particles defining the solid angle for particles (electrons or ions) to access the space between the cylindrical plates. A symmetric potential is applied to the plates creating an electric field such that particles entering the space between the plates are accelerated toward the inner plate. If the incoming particle's energy is such that the centrifugal force experienced by the particle as its trajectory is bent by the electric field equals the electric field force, the particle passes along the gap between the plates, impacts the front end of the channeltron and is counted. Both electron and ion detectors employ post-acceleration (100 V for electrons; 1000 V for ions) to insure unit channeltron efficiency at low energies. The analyzers for ions and electrons are identical except that the polarity on the plates are opposite and the low energy ion apertures are larger than the low energy electron apertures.

Each pair of analyzers consists of one set of cylindrical plates with a radius of curvature of  $60^\circ$  and one set with a radius of curvature of  $127^\circ$ . The  $127^\circ$  detector measures electrons or ions in ten channels equally spaced logarithmically in energy between 30 and 1000 eV. The detector dwells for a period of 98 msec in each channel; 2 msec being left between steps to stabilize the voltage. The plates sequence from high voltage to low. The  $60^\circ$  analyzer measures electrons or ions similarly in 10 channels between 1 keV and 30 keV. The two analyzers are stepped together such that a complete 20 point electron and ion spectrum is returned once per second.

The DMSP satellites are non-spinning. The sensors are mounted on the satellite such that their look directions are oriented radially outward from the Earth at all times. The total package weighs 5 lbs and consumes 0.25 W of power.

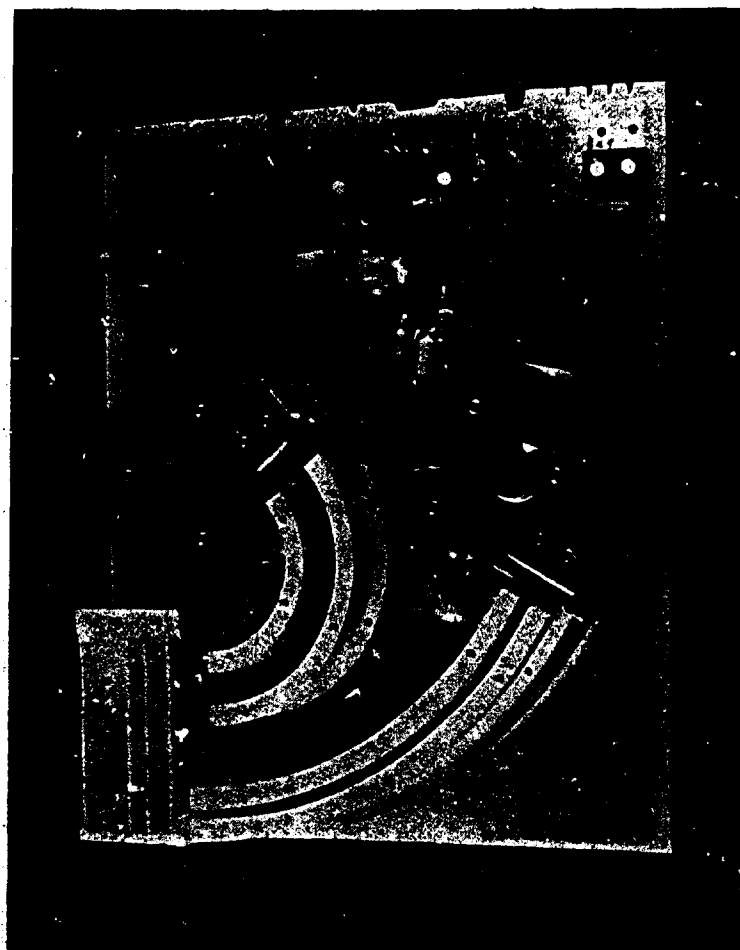


Figure 4. Photograph of One Sensor Head of the SSJ/4 Electrostatic Analyzer

#### **4. ELECTRON DETECTORS: CALIBRATION RESULTS AND CORRECTIONS FOR ELECTRON FLUXES**

Three different facilities were used to calibrate the SSJ/4 sensors for the F6 through F10 DMSP satellites; the electron and ion beam facility at Rice University in Houston, Texas; the electron calibration facility at the Southwest Research Institute in San Antonio, Texas; and a new electron beam calibration system at the Air Force Geophysics Laboratory in Massachusetts. All three facilities employ basically the same technique for producing an electron beam. A metal surface is floated to a high negative potential and illuminated with a monochromatic ultraviolet source. A grounded screen is placed in front of the metal surface and the photoelectrons produced by the ultraviolet light are accelerated away from the surface producing the desired electron beam.



At the Rice and SWRI facilities only limited calibration results were obtained on the F6 SSJ/4 detector. At SWRI, response curves were obtained for electron channels 2, and 6, and ion channel 2. At Rice University, data were obtained only for electron channels 1, 6, 10, and 11, and ion channel 9.

The most complete calibration was obtained using the AFGL facility for the F8 and F10 SSJ/4 detectors. This calibration provided accurate determinations of beam intensity.<sup>15</sup> For this reason we have used the F8 and F10 SSJ/4 calibration data as the basis for deriving the geometric factors for all four detectors. Since all of the detectors are approximately identical this is a reasonable approach. In addition, where data exist we have compared the extrapolated values with those measured at SWRI and Rice University.

In Figures 5 through 7 we show plots comparing some of the values obtained for the energy dependent geometric factor from the three calibration facilities. Figure 5 shows the response curves of the 30 keV channel for F6 measured at Rice, and for F8 and F10 measured at AFGL. Figure 6 shows the curves for the 4.4 keV channel for F6 measured at both Rice and SWRI, and for F10 measured at AFGL. Figure 7 shows the curves for the low energy  $\sim 1$  keV channels for F6 measured at Rice, and F8 and F10 measured at AFGL.

The shapes of the response curves from the three calibrations are in good agreement. In general the peak values of the energy dependent geometric factors are within 20 percent of one another. There are two exceptions: the SWRI results for the 4.4 keV channel give a peak value 30 percent higher than the other two measurements (Figure 6); and the peak value for the high energy head,  $\sim 1$  keV channel obtained at Rice is 36 percent lower than the other two values (not shown). Since the rest of the values agree so well we attribute the disagreement for these two cases to problems with the calibration systems during the runs and not to real differences in the detectors' responses. The peak energies agree within a few percent which is consistent with the accuracy with which the plate voltages for each channel were assigned, and are in good agreement with the central energies predicted on the basis of the plate voltages measured during testing.

---

15. Marshall, F. J., Hardy, D. A., Huber, A., McGarity, J., Pantazis, J., and Winningham, D. (1984) A calibration system for electrostatic analyzers in the energy range (0 - 50 keV), manuscript in preparation for submission to Rev. of Sci. Instru.

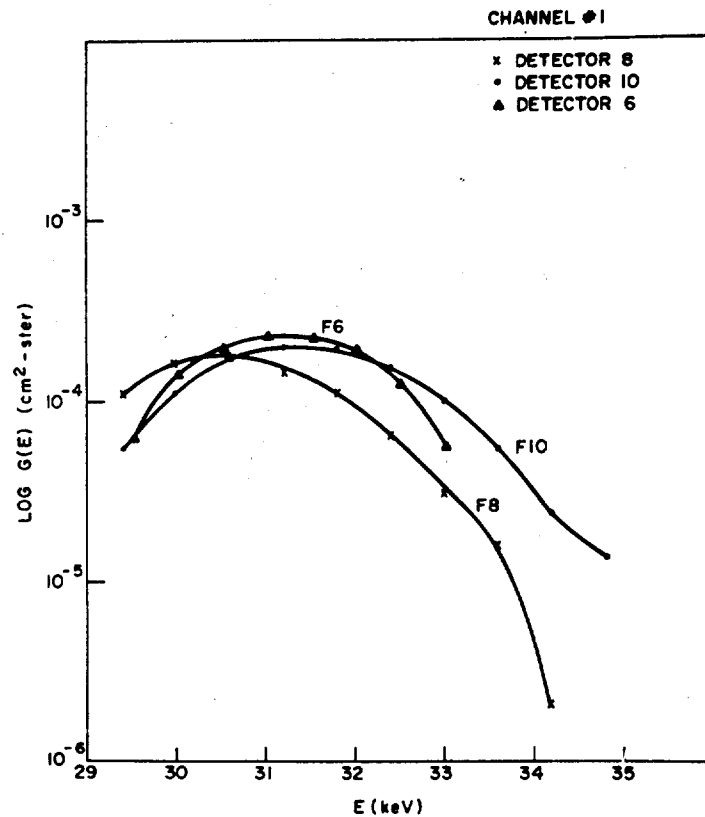


Figure 5. The Energy Dependent Geometric Factor  $G(E)$ , Plotted as a Function of Energy for Channel 1 for Detectors F6 (Rice), F8, and F10 (AFGL)

The agreement of the measurements of the shape of the response both for different channels determined at one facility and between different facilities is shown in Figures 8 through 10. The figures give, respectively, the normalized curves for: channels 1, 6, and 10 for the F6 detector as measured at Rice University; channels 1, 2, 4, 6, 8, and 10 for the F10 detector as measured at AFGL; and some of the low energy channels for F10, channel 11 of F8 measured at AFGL, and channel 11 of F6 measured at Rice. The curves were calculated by normalizing the measurements of  $G(E)$  obtained for a specific channel to the peak value of  $G(E)$  for that channel and by normalizing the energy at which each measurement was made to the central energy,  $E_{\text{peak}}$ , of the channel.

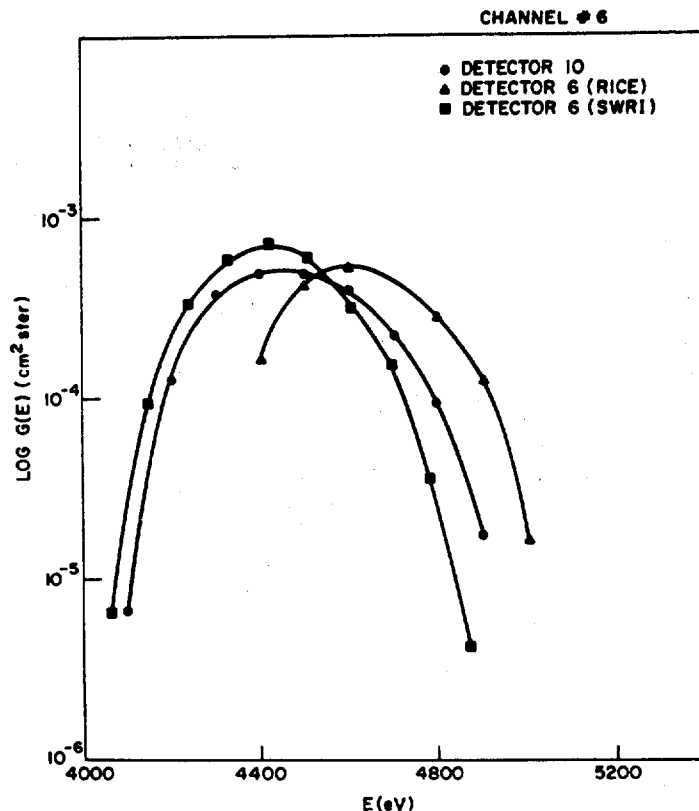


Figure 6. The Energy Dependent Geometric Factor,  $G(E)$ , Plotted as a Function of Energy for Channel 6 for Detectors F6 (Rice), F6 (SWRI), and F10 (AFGL)

The angular acceptance of the detectors was determined by looking at the response of channels 10 and 11 for F6 (Rice), F8, and F10 at approximately their central energies in directions perpendicular and parallel to the two cylindrical plates of the analyzer. The two angles,  $\alpha$  and  $\beta$ , are shown in Figure 11 and the response curves for variations in both angles are shown in Figure 12. In the figures the response curves are normalized to the counts observed where  $\alpha = \beta = 0$  and the results for all of the detectors are superimposed.  $\Delta\alpha$  and  $\Delta\beta$  are defined as the full width half maximum of the angular response; the values for  $\Delta\alpha$  and  $\Delta\beta$  for the three detectors are found in Table 1. There is good agreement between the results for the three detectors.

Based on the above, the characteristics of the 20 electron channels for the F8 and F10 detectors were determined and are listed in Table 2. In the table we have listed for each channel, the energy at the peak of the response curve, the full width at half maximum of the curve, the peak value of the energy dependent geometric factor and the integrated geometric factor. The values were assigned

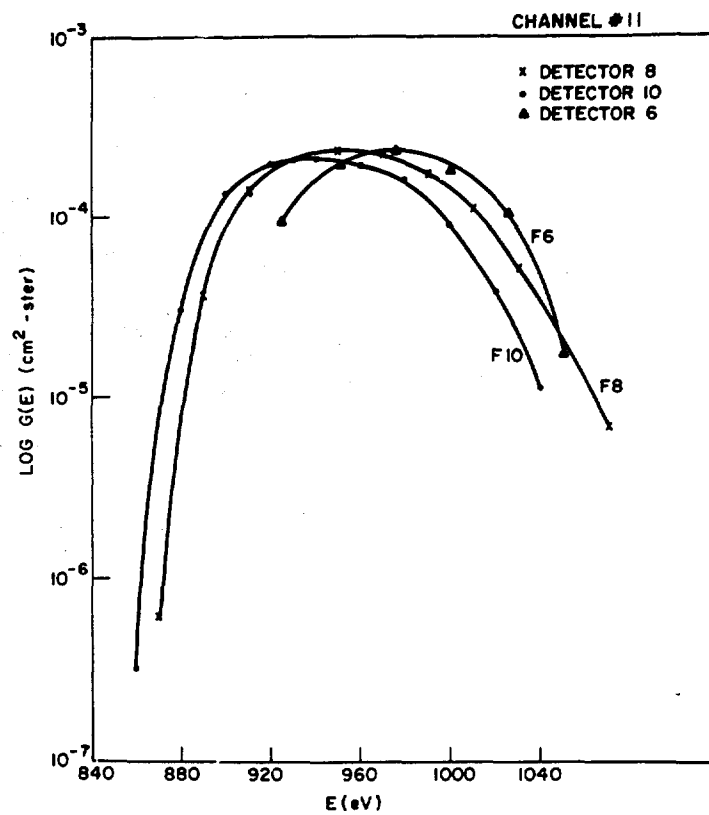


Figure 7. The Energy Dependent Geometric Factor,  $G(E)$ , Plotted as a Function of Energy for Channel 11 for Detectors F6 (Rice), F8, and F10 (AFGL)

as follows: for all channels of both detectors for which response curves were obtained the values were calculated from the curves (starred values). The remaining central energies were assigned from the plate voltages recorded during testing on the ground. The remaining  $\Delta E$ 's were calculated from the average  $\Delta E/E$  of the channels for which the response curves were determined. For the F10 detector the  $G_{\text{peak}}$ 's and integrated geometric factors for the remaining channels were interpolated from the log-log plot of the measured curves (Figures 13 and 14). For the F8 detector, the values of  $G_{\text{peak}}$  and the integrated geometric factor for channels 11 through 20 were assigned by assuming the same energy dependence of the response between 30 eV and 1 keV as measured for the F10 detector and normalizing to the values measured for the F8 detector in channel 11. The values for the remaining low energy values were interpolated as for the F10 detector, from the log-log plot shown in Figure 15.

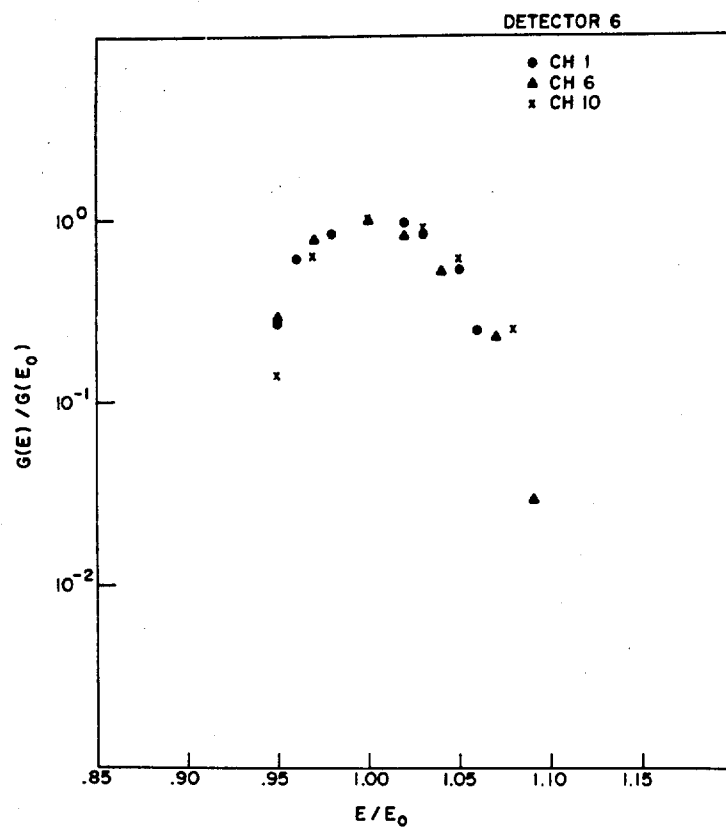


Figure 8. The Energy Dependent Geometric Factor,  $G(E)$ , Normalized to the Peak Geometric Factor,  $G(E)_{\text{peak}}$ , Plotted as a Function of the Energy Normalized to the Channel's Central Energy,  $E_{\text{peak}}$ . This figure shows channels 1, 6, and 10 of detector F6 measured at Rice

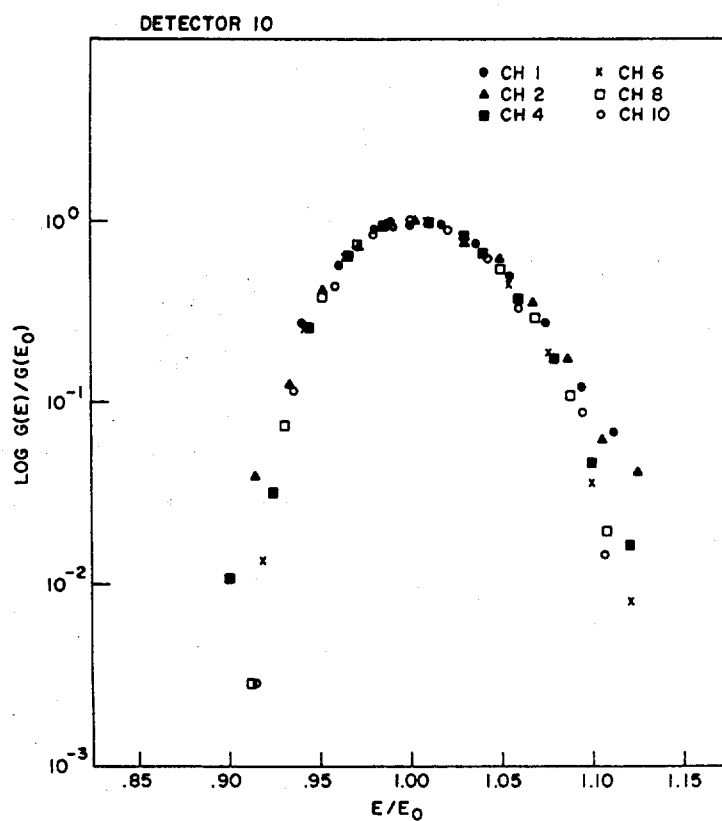


Figure 9. The Energy Dependent Geometric Factor,  $G(E)$ , Normalized to the Peak Geometric Factor,  $G(E)_{\text{peak}}$ , Plotted as a Function of the Energy Normalized to the Channel's Central Energy,  $E_{\text{peak}}$ . This figure shows channels 1, 2, 4, 6, 8, and 10 of detector F10 measured at AFGL

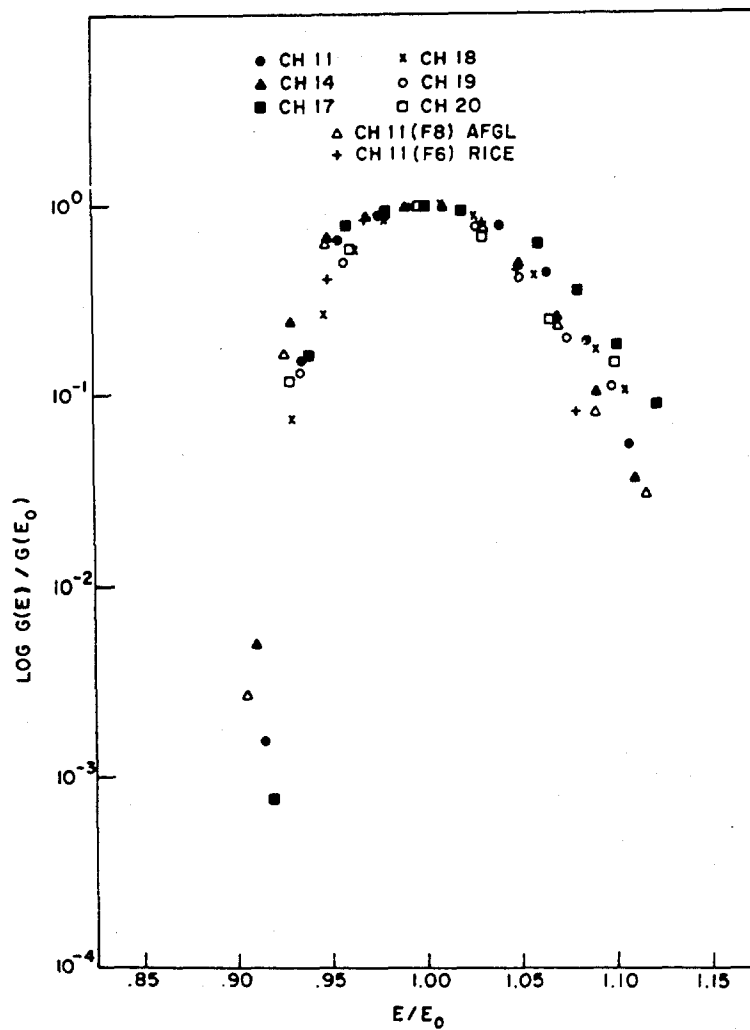


Figure 10. The Energy Dependent Geometric Factor,  $G(E)$ , Normalized to the Peak Geometric Factor,  $G(E)_{\text{peak}}$ , Plotted as a Function of the Energy Normalized to the Channel's Central Energy,  $E_{\text{peak}}$ . This figure shows channels 11, 14, 17, 18, 19, and 20 of detector F10, channel 11 of detector F8, all measured at AFGL and channel 11 of detector F6 measured at Rice

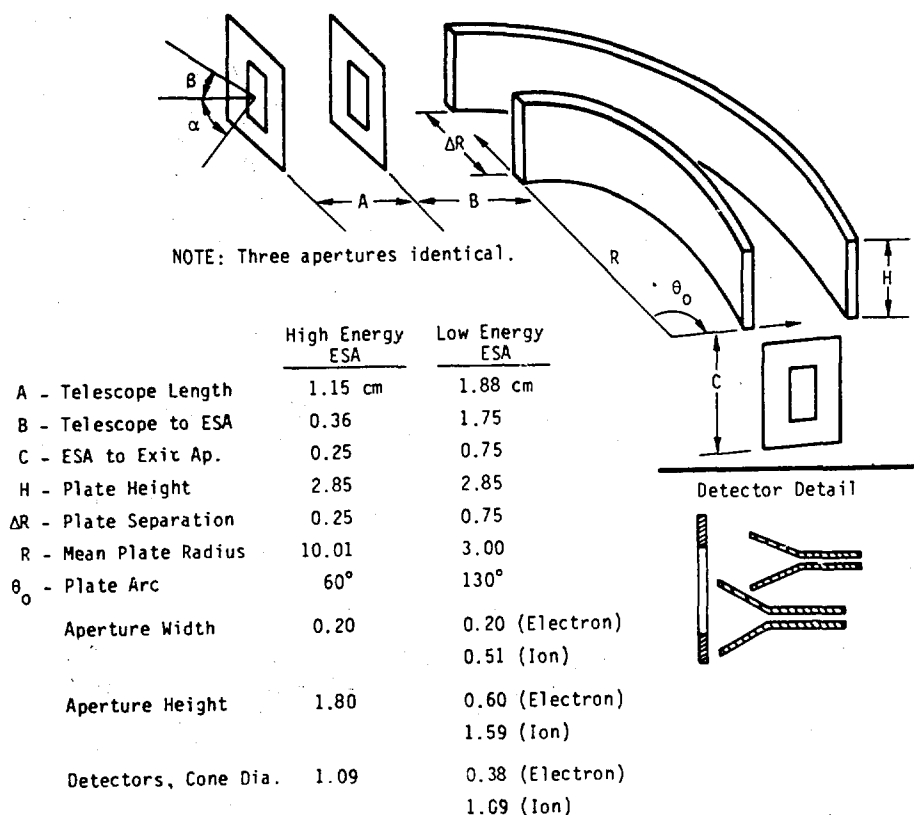


Figure 11. Details of the Configuration of the Apertures and Curved Plates of the Analyzer Showing the Angles  $\alpha$  and  $\beta$

Table 1.  $\Delta\alpha$  and  $\Delta\beta$  for F6, F8, and F10, Channels 10 and 11

$\Delta\alpha$ (channel 10)			$\Delta\alpha$ (channel 11)		
F6	F8	F10	F6	F8	F10
1.7	1.8	2.05	4.3	3.4	3.6
$\Delta\beta$ (channel 10)			$\Delta\beta$ (channel 11)		
F6	F8	F10	F6	F8	F10
5.4	6.8	8.4	5.2	4.7	4.5

\* In the table the values for F6 are from measurements made at Rice and the values for F8 and F10 are from measurements made at AFGL.



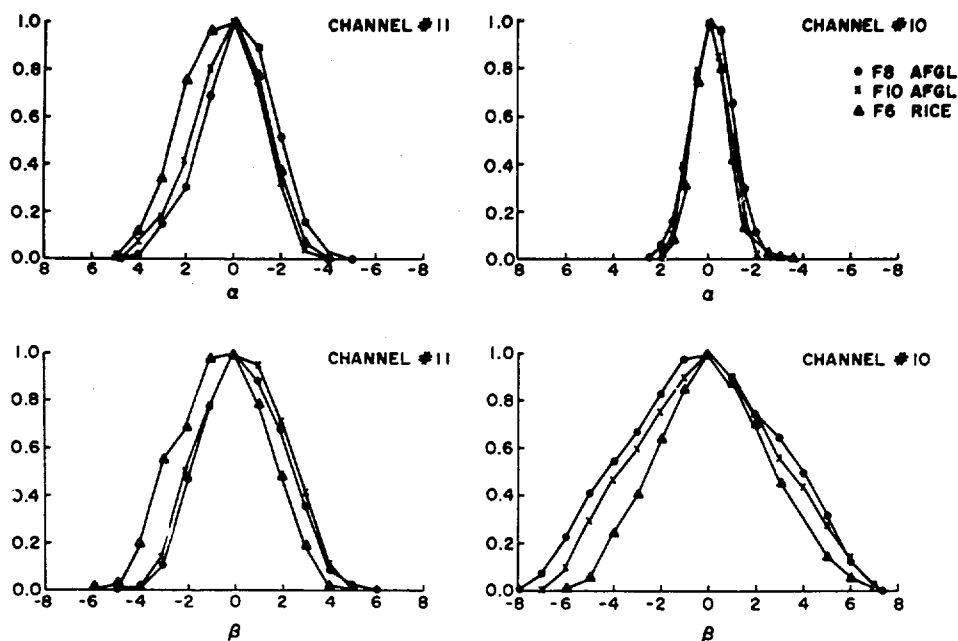


Figure 12. Angular Response of Electron Channels 10 and 11 for the SSJ/4 Detectors for the F6, F8, and 10 Satellites. The top curves give the normalized response for the angle  $\alpha$  with  $\beta = 0$ . The bottom curves show the variation in  $\beta$  with  $\alpha = 0$

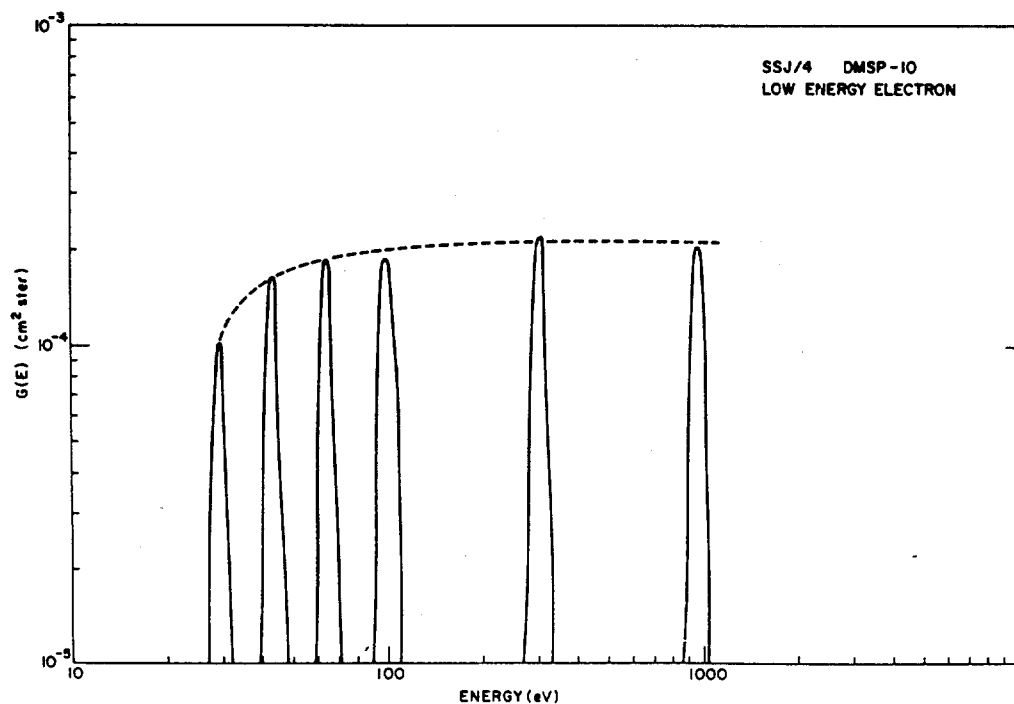


Figure 13. The Logarithm of the Energy Dependent Geometric Factor,  $G(E)$ , of the 6 Calibrated Channels of the Low Energy Electron Analyzer for the F10 Satellite Plotted vs the Logarithm of Energy

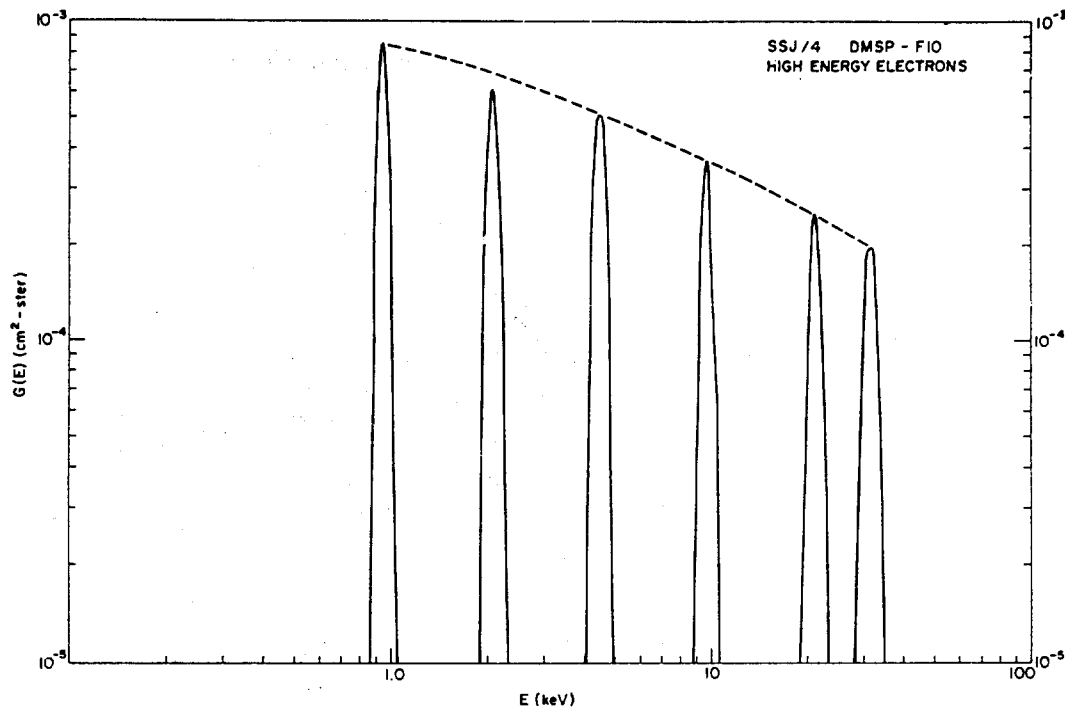


Figure 14. The Logarithm of the Energy Dependent Geometric Factor,  $G(E)$ , of the Calibrated Channels of the High Energy Electron Analyzer for the F10 Satellite Plotted vs the Logarithm of Energy

The values for the F6 and F7 detector electron channels are listed in Table 3. For these detectors the central energies and  $\Delta E$ 's were assigned from the measured plate voltages in the same manner as for the F8 and F10 detectors. The values of  $G_{\text{peak}}$  and the integrated geometric factor are averages of the F8 and F10 detectors' values adjusted for the small differences in average energy. The measured values from the Rice University and SWRI facilities are listed for comparison using the subscripts r and s, respectively.

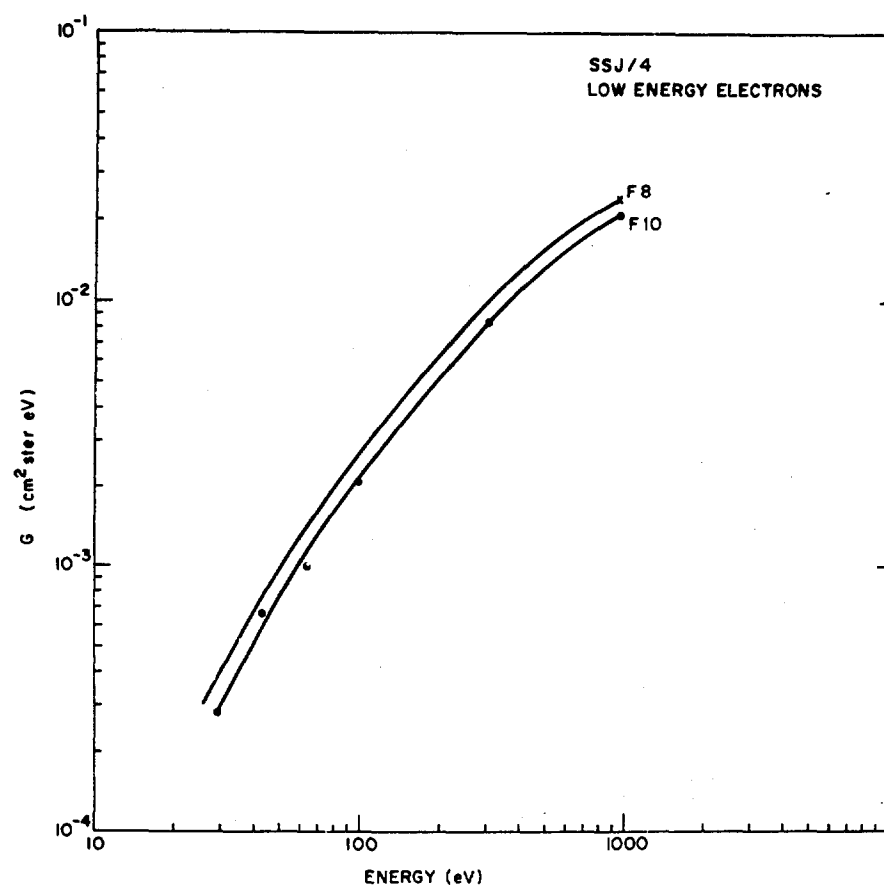


Figure 15. The Logarithm of the Energy Independent Geometric Factor, G, for the Calibrated Channels of the Low Energy Electron Analyzers for the F8 and F10 Satellites Plotted vs the Logarithm of the Energy

Table 2. Derived Electron Geometric Factors for F8 and F10

Ch.	E peak (keV)		$\Delta E$ (keV)		$G(E)_{\text{peak}}$ ( $\text{cm}^2 \text{ ster}$ )		$G$ ( $\text{cm}^2 \text{ ster eV}$ )	
	8	10	8	10	8	10	8	10
1	*30.50	*31.30	*2.90	*3.10	* $1.7 \times 10^{-4}$	* $2.0 \times 10^{-4}$	* $5.1 \times 10^{-1}$	* $6.5 \times 10^{-1}$
2	20.30	21.00	1.93	*2.00	* $2.3 \times 10^{-4}$	* $2.5 \times 10^{-4}$	* $4.4 \times 10^{-1}$	* $5.2 \times 10^{-1}$
3	13.93	13.88	1.32	1.32	* $2.8 \times 10^{-4}$	* $3.1 \times 10^{-4}$	* $3.7 \times 10^{-1}$	* $4.2 \times 10^{-1}$
4	* 9.50	* 9.64	*0.84	*0.88	* $3.4 \times 10^{-4}$	* $3.7 \times 10^{-4}$	* $3.0 \times 10^{-1}$	* $3.5 \times 10^{-1}$
5	6.45	6.46	0.61	0.61	* $4.2 \times 10^{-4}$	* $4.4 \times 10^{-4}$	* $2.5 \times 10^{-1}$	* $2.9 \times 10^{-1}$
6	4.39	* 4.46	0.42	*0.44	* $5.0 \times 10^{-4}$	* $5.1 \times 10^{-4}$	* $2.0 \times 10^{-1}$	* $2.3 \times 10^{-1}$
7	3.01	2.99	0.29	0.28	* $5.8 \times 10^{-4}$	* $5.8 \times 10^{-4}$	* $1.5 \times 10^{-1}$	* $1.7 \times 10^{-1}$
8	2.05	* 2.06	0.195	*0.193	* $6.7 \times 10^{-4}$	* $6.0 \times 10^{-4}$	* $1.2 \times 10^{-1}$	* $1.2 \times 10^{-1}$
9	1.39	1.37	0.132	0.130	* $7.8 \times 10^{-4}$	* $7.6 \times 10^{-4}$	* $9.2 \times 10^{-2}$	* $9.8 \times 10^{-2}$
10	*0.905	*0.940	*0.074	*0.087	* $9.0 \times 10^{-4}$	* $8.4 \times 10^{-4}$	* $6.9 \times 10^{-2}$	* $7.4 \times 10^{-2}$
11	*0.960	*0.940	*0.100	*0.100	* $2.3 \times 10^{-4}$	* $2.1 \times 10^{-4}$	* $2.4 \times 10^{-2}$	* $2.1 \times 10^{-2}$
12	0.670	0.671	0.070	0.070	* $2.3 \times 10^{-4}$	* $2.1 \times 10^{-4}$	* $2.0 \times 10^{-2}$	* $1.7 \times 10^{-2}$
13	0.459	0.459	0.048	0.048	* $2.3 \times 10^{-4}$	* $2.1 \times 10^{-4}$	* $1.5 \times 10^{-2}$	* $1.3 \times 10^{-2}$
14	0.314	*0.300	0.033	*0.031	* $2.3 \times 10^{-4}$	* $2.2 \times 10^{-4}$	* $1.0 \times 10^{-2}$	* $8.3 \times 10^{-3}$
15	0.212	0.215	0.022	0.022	* $2.3 \times 10^{-4}$	* $2.1 \times 10^{-4}$	* $6.8 \times 10^{-3}$	* $5.8 \times 10^{-3}$
16	0.144	0.144	0.0150	0.0150	* $2.2 \times 10^{-4}$	* $2.1 \times 10^{-4}$	* $4.4 \times 10^{-3}$	* $3.6 \times 10^{-3}$
17	0.099	*0.098	0.0103	*0.0110	* $2.1 \times 10^{-4}$	* $1.9 \times 10^{-4}$	* $2.7 \times 10^{-3}$	* $2.1 \times 10^{-3}$
18	0.067	*0.063	0.0070	*0.0061	* $2.0 \times 10^{-4}$	* $1.9 \times 10^{-4}$	* $1.6 \times 10^{-3}$	* $9.9 \times 10^{-4}$
19	0.046	*0.0428	0.0048	*0.0036	* $1.8 \times 10^{-4}$	* $1.7 \times 10^{-4}$	* $8.7 \times 10^{-4}$	* $6.6 \times 10^{-4}$
20	0.032	*0.0291	0.0033	*0.0026	* $1.4 \times 10^{-4}$	* $1.0 \times 10^{-4}$	* $4.6 \times 10^{-4}$	* $2.8 \times 10^{-4}$

Table 3. Derived Electron Geometric Factors for F6 and F7

Ch	E peak (keV)		$\Delta E$ (keV)		$G(E)_{\text{peak}}$ (cm <sup>2</sup> ster)		$G$ (cm <sup>2</sup> ster eV)				
	6	7	6*	6	7	6*	6	7	6*		
1	30.18	30.34	31.0 <sub>r</sub>	2.75	2.76	2.77 <sub>r</sub>	$1.9 \times 10^{-4}$	$1.9 \times 10^{-4}$	$2.3 \times 10^{-4}$	$5.8 \times 10^{-1}$	$7.3 \times 10^{-1}$
2	20.62	20.71	21.8 <sub>s</sub>	1.88	1.89	1.87 <sub>s</sub>	$2.4 \times 10^{-4}$	$2.4 \times 10^{-4}$	$3.1 \times 10^{-4}$	$4.9 \times 10^{-1}$	$5.2 \times 10^{-1}$
3	14.04	14.07		1.28	1.28		$2.9 \times 10^{-4}$	$2.9 \times 10^{-4}$		$4.1 \times 10^{-1}$	
4	9.58	9.57		0.87	0.87		$3.6 \times 10^{-4}$	$3.6 \times 10^{-4}$		$3.3 \times 10^{-1}$	
5	6.50	6.57		0.59	0.60		$4.3 \times 10^{-4}$	$4.3 \times 10^{-4}$		$2.7 \times 10^{-1}$	
6	4.42	4.47	4.6 <sub>r,s</sub>	0.40	0.41	0.37 <sub>r</sub> 0.35 <sub>s</sub>	$5.0 \times 10^{-4}$	$5.0 \times 10^{-4}$	$5.6 \times 10^{-4}$ $6.9 \times 10^{-4}$	$2.1 \times 10^{-1}$	$2.1 \times 10^{-1}$ $2.4 \times 10^{-1}$
7	3.05	3.05		0.28	0.28		$5.7 \times 10^{-4}$	$5.7 \times 10^{-4}$		$1.6 \times 10^{-1}$	
8	2.06	2.10		0.19	0.19		$6.6 \times 10^{-4}$	$6.6 \times 10^{-4}$		$1.3 \times 10^{-1}$	
9	1.41	1.43		0.13	0.13		$7.6 \times 10^{-4}$	$7.6 \times 10^{-4}$		$9.5 \times 10^{-2}$	
10	0.984	0.985	0.98 <sub>r</sub>	0.09	0.09	0.088 <sub>r</sub>	$8.6 \times 10^{-4}$	$8.6 \times 10^{-4}$	$5.6 \times 10^{-4}$	$7.6 \times 10^{-2}$	$7.6 \times 10^{-2}$
11	0.992	0.995	0.97 <sub>r</sub>	0.100	0.101	0.091 <sub>r</sub>	$2.2 \times 10^{-4}$	$2.2 \times 10^{-4}$	$2.3 \times 10^{-4}$	$2.3 \times 10^{-2}$	$2.3 \times 10^{-2}$
12	0.679	0.679		0.069	0.069		$2.3 \times 10^{-4}$	$2.3 \times 10^{-4}$		$1.8 \times 10^{-2}$	
13	0.462	0.462		0.047	0.047		$2.3 \times 10^{-4}$	$2.3 \times 10^{-4}$		$1.4 \times 10^{-2}$	
14	0.317	0.314		0.032	0.032		$2.2 \times 10^{-4}$	$2.2 \times 10^{-4}$		$9.6 \times 10^{-3}$	
15	0.213	0.215		0.022	0.022		$2.2 \times 10^{-4}$	$2.2 \times 10^{-4}$		$6.3 \times 10^{-3}$	
16	0.145	0.147		0.0147	0.0149		$2.1 \times 10^{-4}$	$2.1 \times 10^{-4}$		$4.0 \times 10^{-3}$	
17	0.100	0.100		0.0101	0.0101		$2.1 \times 10^{-4}$	$2.1 \times 10^{-4}$		$2.4 \times 10^{-3}$	
18	0.068	0.069		0.0069	0.0070		$2.0 \times 10^{-4}$	$2.0 \times 10^{-4}$		$1.4 \times 10^{-3}$	
19	0.046	0.047		0.0047	0.0048		$1.8 \times 10^{-4}$	$1.8 \times 10^{-4}$		$7.3 \times 10^{-4}$	
20	0.032	0.032		0.0032	0.0032		$1.3 \times 10^{-4}$	$1.3 \times 10^{-4}$		$4.0 \times 10^{-4}$	

## 5. ION DETECTORS: CALIBRATION RESULTS AND CORRECTIONS FOR ELECTRON FLUXES

### 5.1 Derived Ion Geometric Factors

A combination of electron calibration results and in-flight data were used to assign ion geometric factors. Only a small amount of ion calibration data was obtained as a result of limited availability of ion calibration facilities and difficulties encountered during operation at the ones used. This approach is possible because the electron and ion detectors are identical except that the plate polarity has been reversed and the opening aperture for the low energy ion detector increased.

To assign the characteristics for the high energy ion channels we used two facts. First, since the electron and ion detectors are identical except for the change in plate voltage polarity, the electrons and ion channels should have the same peak geometric factor and shape at the ~1 keV channel where the efficiency of the channel-tron for both electrons and ions is unity. Second, the efficiency of the ion channel should be unity at all energies between 1 keV and 30 keV. Since the shape of the response curve will be the same for electrons and ions, the  $\Delta E$ 's were assigned using the average value of  $\Delta E/E$  from the F8 and F10 detectors.  $G_{\text{peak}}$  for all high energy channels was taken to be the average value of the electron channels at 1 keV for the F8 and F10 detectors. The integrated geometric factors were then calculated using this peak value and assuming the average normalized shape determined for the electron channels.

Assigning the characteristics for the low energy ion head is more difficult due to the differences in the dimensions of the aperture for electrons and ions. To first order, however, the shape of the response curve is dependent on the curvature and spacing of cylindrical curved plates and not the aperture dimensions. Therefore, we can assign the peak energies and  $\Delta E$ 's as we have for electrons.

To assign  $G_{\text{peak}}$  and the integrated geometric factor we used ion flight data. Since the low and high energy heads both have a channel at 1 keV, in flight these two channels should record counts proportional to the ratio of their respective  $G_{\text{peak}}$  values times the full width at half maximum:

$$\frac{\text{CNTS}_{11}}{\text{CNTS}_{10}} = \frac{(G_{\text{peak}})_{11} \Delta E_{11}}{(G_{\text{peak}})_{10} \Delta E_{10}} = \text{constant} . \quad (1)$$

The average value of this ratio can be determined using on orbit data, and since the  $\Delta E$ 's have already been specified and  $G_{\text{peak}}$  for the high energy head is known,  $G_{\text{peak}}$  for the low energy 1 keV channel can be determined.

Background counts within the ion detector can obscure true counts in regions of low fluxes, therefore we used ion data in the diffuse auroral regions where the count levels are typically greater than 100 in the low energy detector, thus minimizing the error due to background counts. Data were chosen randomly (19 February 1983, 26 February 1983, and 4 April 1983 for F6, and 25 November 1983 and 15 January 1984 for F7) subject to the criterion that the DMSP precipitation profiles exhibited a smoothing varying integral flux (JTOT) across the diffuse auroral region. Ion counts were summed over 10-sec intervals within the diffuse aurora. The ion count ratio was then calculated by dividing the counts in channel 11 by the counts in channel 10. A total of 349 10-sec intervals were used to determine the F6 ion ratios. The average of the ratio of ion counts in channel 10 to channel 11 is ~42. Sixty-five 10-sec averages were performed to determine the ratios for F7. The average of the ratios of ion counts in channel 11 to channel 10 is ~28. Using these ratios  $G_{\text{peak}}$  for channel 11 was determined. Since the ion detector has a post acceleration of 1 keV the efficiency at all low energy channels can be taken to be unity and the same  $G_{\text{peak}}$  applied. Using the known shape of the response curves the integrated geometric factors were then determined. The results are shown in Table 4.

Using the values in Tables 2, 3, and 4, the count rates of the SSJ/4 detectors can be converted to differential flux using the equation

$$J(E_i) = \frac{C_i / \Delta T}{G(E_i)}, \quad (2)$$

where  $C_i$  is the number of counts detected by the channeltron with central energy  $E_i$ ,  $\Delta T$  is the accumulation time, equal to 98 msec,  $G(E_i)$  is the energy independent geometric factor for channel  $i$  in  $\text{cm}^2 \text{ ster eV}$ .

## 5.2 Corrections for Electron Fluxes

In order to obtain a large geometric factor for the low energy ion detector the cross-sectional areas of the front and rear apertures of the detectors were increased by approximately a factor of 10 each over those of low energy electron detector. While this produced the desired result of increased sensitivity it also left the detector susceptible to some contamination from the scattering of electrons through the sensor. To quantify this effect the ion channel angular response to various electron energies was measured to determine their energy dependent geometric factor,  $G_i(E_e)$ , to electrons. For completeness, the  $G_i(E_e)$ 's for both low and high energy ion channels were determined although since the high energy detector's geometric factor is much smaller than that of the low energy detector the degree of contamination is smaller. The experimental results of  $G_i(E_e)$  for four channels of the low

Table 4. Derived Ion Geometric Factors for F6 and F7

Ch	E <sub>peak</sub> (keV)			ΔE (keV)			G(E) <sub>peak</sub> (cm <sup>2</sup> ster)			G (cm <sup>2</sup> ster eV)		
	6	7	8*	6	7	8*	6	7	8*	6	7	8*
1	30.18	30.34		2.75	2.76		8.6 × 10 <sup>-4</sup>	8.6 × 10 <sup>-4</sup>		2.4 × 10 <sup>-0</sup>	2.4 × 10 <sup>-0</sup>	
2	20.62	20.71	21.05 <sub>s</sub>	1.88	1.89	1.71 <sub>s</sub>	8.6 × 10 <sup>-4</sup>	8.6 × 10 <sup>-4</sup>		1.6 × 10 <sup>-0</sup>	1.6 × 10 <sup>-0</sup>	6.2 × 10 <sup>-1</sup>
3	14.04	14.07		1.28	1.28		8.6 × 10 <sup>-4</sup>	8.6 × 10 <sup>-4</sup>		1.1 × 10 <sup>-0</sup>	1.1 × 10 <sup>-0</sup>	
4	9.58	9.57		0.87	0.87		8.6 × 10 <sup>-4</sup>	8.6 × 10 <sup>-4</sup>		7.6 × 10 <sup>-1</sup>	7.5 × 10 <sup>-1</sup>	
5	6.50	6.57		0.59	0.60		8.6 × 10 <sup>-4</sup>	8.6 × 10 <sup>-4</sup>		5.1 × 10 <sup>-1</sup>	5.2 × 10 <sup>-1</sup>	
6	4.42	4.47	4.6 <sub>s</sub>	0.40	0.41	0.34 <sub>s</sub>	8.6 × 10 <sup>-4</sup>	8.6 × 10 <sup>-4</sup>		3.5 × 10 <sup>-1</sup>	3.5 × 10 <sup>-1</sup>	2.8 × 10 <sup>-1</sup>
7	3.05	3.05		0.28	0.28		8.6 × 10 <sup>-4</sup>	8.6 × 10 <sup>-4</sup>		2.4 × 10 <sup>-1</sup>	2.4 × 10 <sup>-1</sup>	
8	2.06	2.10		0.19	0.19		8.6 × 10 <sup>-4</sup>	8.6 × 10 <sup>-4</sup>		1.6 × 10 <sup>-1</sup>	1.7 × 10 <sup>-1</sup>	
9	1.41	1.43	1.48 <sub>r</sub>	0.13	0.13	0.10 <sub>r</sub>	8.6 × 10 <sup>-4</sup>	8.6 × 10 <sup>-4</sup>		1.1 × 10 <sup>-1</sup>	1.1 × 10 <sup>-1</sup>	1.0 × 10 <sup>-1</sup>
10	0.984	0.985		0.090	0.090		8.6 × 10 <sup>-4</sup>	8.6 × 10 <sup>-4</sup>		7.6 × 10 <sup>-2</sup>	7.6 × 10 <sup>-2</sup>	
11	0.992	0.995		0.100	0.101		3.2 × 10 <sup>-2</sup>	2.2 × 10 <sup>-2</sup>		3.2 × 10 <sup>-0</sup>	2.1 × 10 <sup>-0</sup>	
12	0.679	0.679		0.069	0.069		3.2 × 10 <sup>-2</sup>	2.2 × 10 <sup>-2</sup>		2.2 × 10 <sup>-0</sup>	1.4 × 10 <sup>-0</sup>	
13	0.462	0.462		0.047	0.047		3.2 × 10 <sup>-2</sup>	2.2 × 10 <sup>-2</sup>		1.5 × 10 <sup>-0</sup>	9.8 × 10 <sup>-1</sup>	
14	0.317	0.314		0.032	0.032		3.2 × 10 <sup>-2</sup>	2.2 × 10 <sup>-2</sup>		1.0 × 10 <sup>-0</sup>	6.6 × 10 <sup>-1</sup>	
15	0.213	0.215		0.022	0.022		3.2 × 10 <sup>-2</sup>	2.2 × 10 <sup>-2</sup>		7.0 × 10 <sup>-1</sup>	4.6 × 10 <sup>-1</sup>	
16	0.145	0.147		0.0147	0.0149		3.2 × 10 <sup>-2</sup>	2.2 × 10 <sup>-2</sup>		4.7 × 10 <sup>-1</sup>	3.1 × 10 <sup>-1</sup>	
17	0.100	0.100		0.0101	0.0101		3.2 × 10 <sup>-2</sup>	2.2 × 10 <sup>-2</sup>		3.2 × 10 <sup>-1</sup>	2.1 × 10 <sup>-1</sup>	
18	0.068	0.069		0.0069	0.0070		3.2 × 10 <sup>-2</sup>	2.2 × 10 <sup>-2</sup>		2.2 × 10 <sup>-1</sup>	1.5 × 10 <sup>-1</sup>	
19	0.046	0.047		0.0047	0.0048		3.2 × 10 <sup>-2</sup>	2.2 × 10 <sup>-2</sup>		1.5 × 10 <sup>-1</sup>	1.0 × 10 <sup>-1</sup>	
20	0.032	0.032		0.0032	0.0032		3.2 × 10 <sup>-2</sup>	2.2 × 10 <sup>-2</sup>		1.1 × 10 <sup>-1</sup>	7.0 × 10 <sup>-2</sup>	



energy head of the F10 ion detector (ions with energy between 30 and 1000 eV) are plotted in Figure 16. Smooth curves drawn using the data points form the electron rejection curves. Corresponding values of  $G_i(E_e)$  for four channels of the F10 high energy head (ions with energy between 1 and 30 keV) are shown in Figure 17.

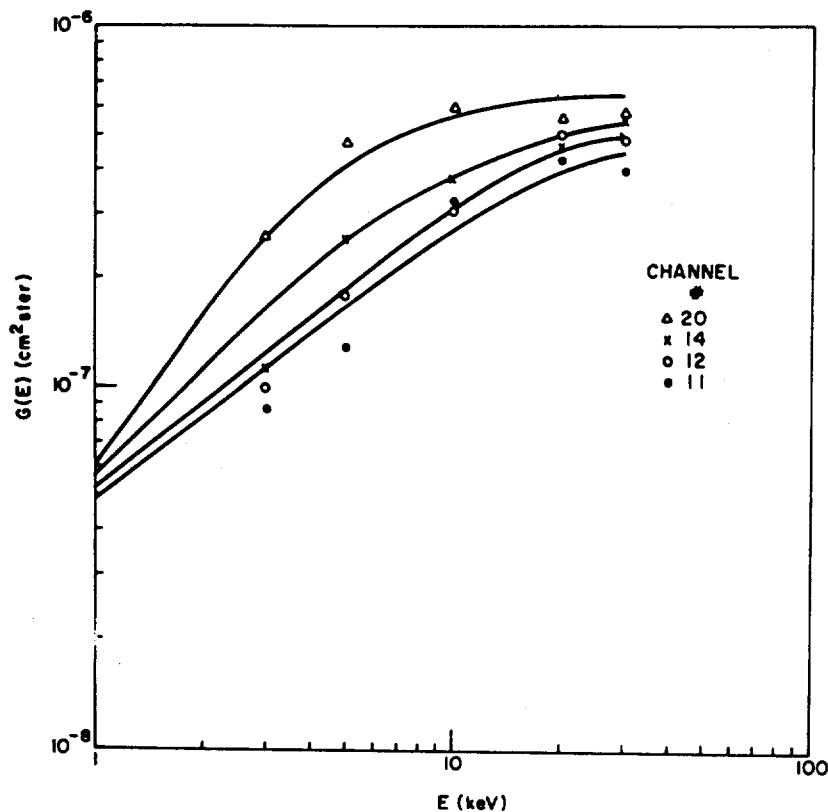


Figure 16. The Logarithm of the Energy Dependent Geometric Factor for Four of the Low Energy Channels of the Ion Analyzer to Electrons for the F10 Satellite Plotted vs the Logarithm of the Energy. The four solid lines give an approximate fit to the measurements in each channel

The electron rejection curves illustrate that the values of  $G_i(E_e)$  increase with increasing energy of electrons and asymptotically either reach the value of  $(4-6) \times 10^{-7} \text{ cm}^2 \text{ ster}$  or slightly fall off from this value when the energy of electrons is beyond 20 keV. As expected, the contamination from electrons is greatest in the lowest energy channels of the ion detector (that is,  $G_i(E_e)$  is larger for channel 20 than for channel 11). A complete set of  $G_i(E_e)$  values for the ten

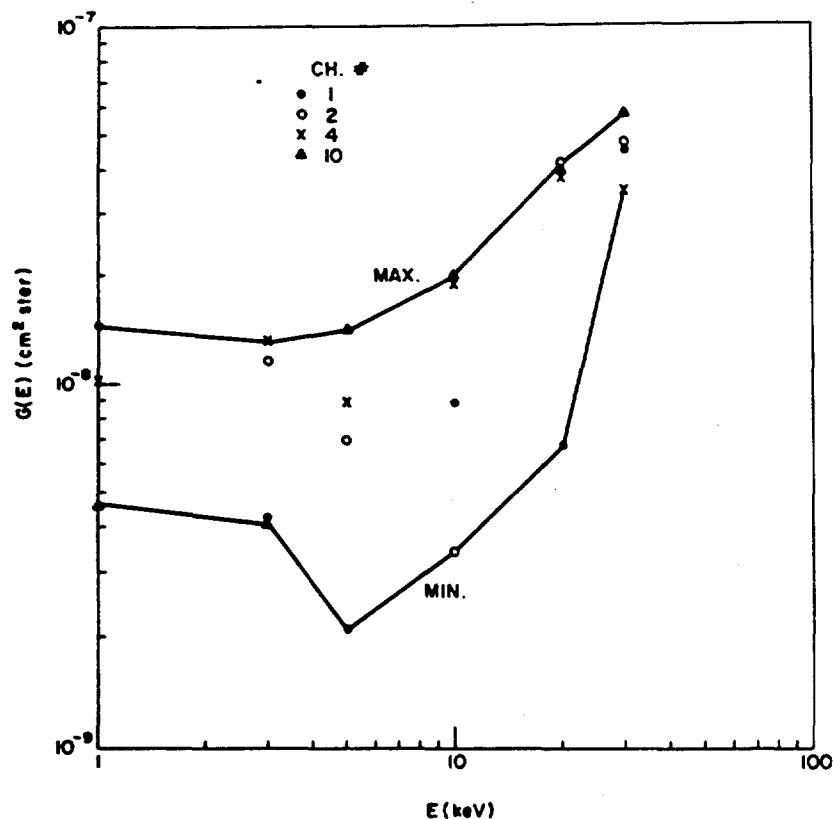


Figure 17. The Logarithm of the Maximum and Minimum Energy Dependent Geometric Factors for the High Energy Channels of the Ion Analyzers to Electrons for the F10 Satellite Plotted vs the Logarithm of the Energy

energy channels of the low energy head of the ion detector is obtained by means of linear interpolation from the electron rejection curves shown in Figure 16.

The values of  $G_i(E_e)$  for the channels of the high energy head of the ion detector are too scattered to be fitted with a smooth rejection curve. Nevertheless these measurements all indicate that the high energy ion detector is less sensitive than the low energy detector to contamination from electrons with energy between 3 and 10 keV (see Figure 17). In general, the value of  $G_i(E_e)$  for the high energy head is at least an order of magnitude smaller than the  $G_i(E_e)$  value for the low energy head. Instead of trying to interpolate the rejection curve for each high energy ion channel we chose the values of maximum  $G(E_n)$  from measurements of four high energy channels (where  $E_n$  is the step energy of the electron beam) to construct the maximum rejection curve and the values of minimum  $G(E_n)$  to form the minimum rejection curve. The values of ten rejection curves for the low energy head and two rejection curves for the high energy head of the ion detectors are listed in

Table 5. The maximum  $G(E_n)$  curve was used to calculate the contamination in all high energy ion channels. These values are then used with Eq. (3) to calculate the counts contributed by the electrons that scatter through the  $i$ th channel of the ion detector.

$$C_{RJ} \text{ (count/sec)} = \int J(E)G(E)dE ; \quad (3)$$

$$C_{RJ} \approx J(E_1)G_i(E_1)(E_1 - E_2)/2 + \sum_{j=2}^9 J(E_j)G_i(E_j)(E_{j-1} - E_{j+1})/2 \\ + J(E_{10})G_i(E_{10})(E_9 - E_{10})/2 ;$$

where  $J(E_j)$  is the measured differential flux of precipitating electrons of energy  $E_j$ . Equation (3) should give a good estimate of rejected counts (that is,  $C_{RJ}$ ) if the spectrum of precipitating electron flux is falling with energy at the high energy limit of the detector.

Electron contamination of the ion counts has been found to range from being insignificant to being so large that it obscures all real ion counts. The range depends on the level and energy of both electron and ion fluxes and is not easily categorized. However, we can say that the correction for electron contamination must be made in intense, energetic electron events, such as inverted-V's. For diffuse aurora the correction is in the neighborhood of 10 percent. Examples of the use of the electron rejection curves will be given in the next section.

## 6. USES OF THE SSJ/4 DATA

In this section we demonstrate uses of the SSJ/4 data using precipitating electron and ion data from north pole passes made by the F6 satellite on 10 and 21 January 1983. First, the quantities used for survey plots of the data are defined. Second, the general features of the precipitation in the auroral oval, along the satellite track, are discussed for a pass on 10 January 1983. The two-dimensional view of visible features from the scanning radiometer for this pass is given in Figure 1 in Section 1. Third, examples are given of the use of the electron rejection curves to obtain the correct ion spectra in discrete auroral features. Fourth, the low ion counts in the polar cap are averaged to determine a real, but extremely weak signal of thermal, warm precipitation.

Table 5. Rejection Curve Values

$G_1(E_e) \text{ cm}^2 \text{ ster (for the low energy head)}$										
$E_e \text{ (keV)}$	Ch 11	Ch 12	Ch 13	Ch 14	Ch 15	Ch 16	Ch 17	Ch 18	Ch 19	Ch 20
(1) 30.180	4.5(-7)	5.1(-7)	5.2(-7)	5.3(-7)	5.7(-7)	5.9(-7)	6.0(-7)	6.1(-7)	6.2(-7)	6.3(-7)
(2) 20.620	4.0(-7)	4.6(-7)	4.8(-7)	5.0(-7)	5.4(-7)	5.7(-7)	5.9(-7)	6.0(-7)	6.1(-7)	6.2(-7)
(3) 14.040	3.4(-7)	3.8(-7)	4.2(-7)	4.4(-7)	5.0(-7)	5.4(-7)	5.7(-7)	5.9(-7)	6.0(-7)	6.1(-7)
(4) 9.580	2.7(-7)	3.0(-7)	3.4(-7)	3.8(-7)	4.4(-7)	4.9(-7)	5.2(-7)	5.4(-7)	5.6(-7)	5.7(-7)
(5) 6.500	2.0(-7)	2.3(-7)	2.7(-7)	3.0(-7)	3.7(-7)	4.1(-7)	4.4(-7)	4.6(-7)	4.7(-7)	4.8(-7)
(6) 4.420	1.5(-7)	1.6(-7)	2.0(-7)	2.3(-7)	2.8(-7)	3.1(-7)	3.4(-7)	3.5(-7)	3.6(-7)	3.7(-7)
(7) 3.050	1.1(-7)	1.2(-7)	1.5(-7)	1.7(-7)	2.0(-7)	2.2(-7)	2.4(-7)	2.5(-7)	2.6(-7)	2.6(-7)
(8) 2.060	8.3(-8)	9.0(-8)	1.1(-7)	1.2(-7)	1.3(-7)	1.4(-7)	1.5(-7)	1.5(-7)	1.5(-7)	1.6(-7)
(9) 1.410	6.2(-8)	6.8(-8)	7.4(-8)	7.8(-8)	8.2(-8)	8.5(-8)	8.6(-8)	8.8(-8)	8.8(-8)	8.9(-8)
(10) 0.984	4.7(-8)	5.0(-8)	5.1(-8)	5.2(-8)	5.3(-8)	5.4(-8)	5.4(-8)	5.5(-8)	5.5(-8)	5.5(-8)

$G_1(E_e) \text{ cm}^2 \text{ ster (for the high energy head)}$			
$E_e \text{ (keV)}$	$G_1(E_e) \text{ max}$	$G_1(E_e) \text{ min}$	
(1) 30.180	5.7(-8)	3.5(-8)	
(2) 20.620	4.2(-8)	7.2(-9)	
(3) 14.040	2.8(-8)	4.7(-9)	
(4) 9.580	1.9(-8)	3.3(-9)	
(5) 6.500	1.6(-8)	2.5(-9)	
(6) 4.420	1.4(-8)	2.5(-9)	
(7) 3.050	1.3(-8)	4.1(-9)	
(8) 2.060	1.4(-8)	4.3(-9)	
(9) 1.410	1.4(-8)	4.4(-9)	
(10) 0.984	1.5(-8)	4.6(-9)	

## 6.1 Survey Plots

For each satellite pass the following quantities are calculated and plotted as a function of universal time for a data survey:

(a) The total number flux or integral flux JTOT is

$$JTOT = \sum_i J(E_i) \frac{(E_{i-1} - E_{i+1})}{2} \quad (4)$$

where  $J(E_i)$  is the differential number flux for each energy channel with central energy  $E_i$ . JTOT is measured in particles/(cm<sup>2</sup> ster sec),

(b) The integral energy flux, JETOT, is

$$JETOT = \sum_i E_i J(E_i) \frac{(E_{i-1} - E_{i+1})}{2} \quad (5)$$

JETOT is measured in keV/(cm<sup>2</sup> ster sec).

(c) The average energy, EAVE, is

$$EAVE = \frac{JETOT}{JTOT} \quad (6)$$

EAVE is measured in keV.

Figure 18 is an example of survey plots for electrons (18a) and ions (18b) during a north polar pass of the F6 satellite on 10 January 1983, from 15:32 - 15:57 UT. The universal time is given in seconds with an interval of one minute between tick marks. At 2-min intervals ephemeris data are given. The ephemerides given are the geographic coordinates of the satellite (GLAT and GLON); the corrected geomagnetic coordinates of the satellites (MLAT, MLON), which are projected along the magnetic field line to 110 km; and the magnetic local time (MLT). The integral and energy flux values are plotted on log scales; the average energy is plotted on a linear scale. During this pass the magnetic activity as measured by KP was moderate, 3-. However, very high activity characterized the first half of the day (7+, 8+, 7, 5). The satellite crosses the high latitude region from ~04 magnetic local time (MLT), or predawn to 19 MLT or post-dusk. The survey plot shows the morning diffuse auroral precipitation rising out of an equatorward background. On the poleward edge of the electron diffuse aurora the electron precipitation is intense and structured, producing discrete auroral forms in a westward traveling surge. Very low fluxes mark clear entry into the polar cap. After ~8 min in the cap the satellite again crosses the auroral oval, now on the eveningside. The evening oval is narrow and the particle precipitation weaker than that on the morningside.

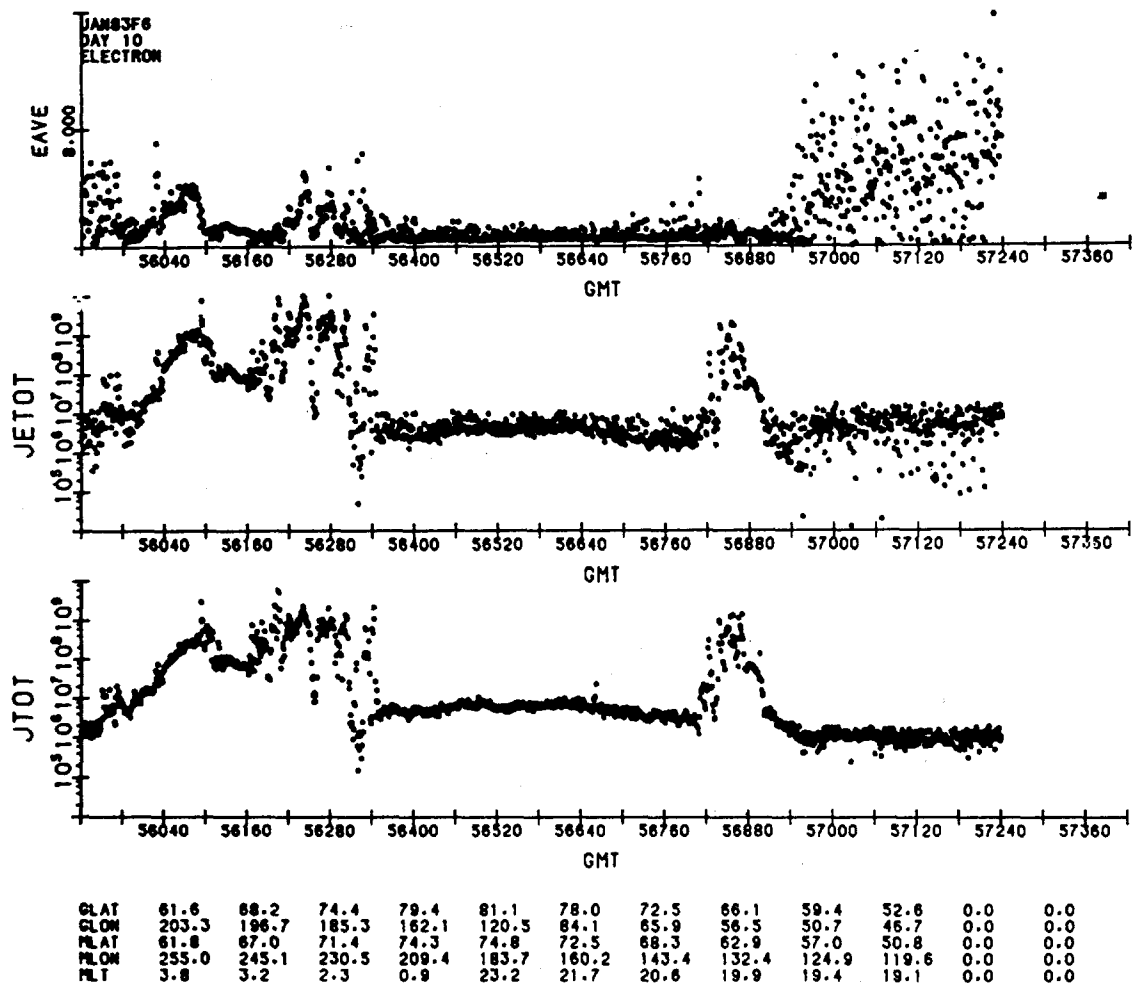


Figure 18a. Electron Data From a Northern Hemisphere Pass of the F6 Satellite Occurring Between 15:32 UT (55,920 sec) and 15:27 UT (57,420 sec) on 10 January 1983. For both electrons and ions the three panels give, from top to bottom, the average energy of the particles, EAVE, in units of keV plotted on a linear scale; the integrated energy flux, JETOT, in units of keV/cm<sup>2</sup>-sec-ster plotted on a logarithmic scale; and the integrated number flux, JTOT, in units of electrons/cm<sup>2</sup>-sec-ster plotted on a logarithmic scale. The bottom of each figure is annotated with the time in universal seconds, the geographic and geomagnetic coordinates of the satellite mapped down to the field lines to 110 km, and the geomagnetic local time



## 6.2 Auroral Electron and Ion Boundaries

The boundaries in particle precipitation that are observed at low altitude result from two types of processes. The first are the restrictions on the particle trajectories for plasma in the inner magnetosphere resulting from the combined action of the convection electric field, the gradient and curvature magnetic field drifts, and the requirement for overall charge neutrality. These restrictions define a minimum radial distance in the magnetic equatorial plane to which the plasma can penetrate and which can map to low altitudes as the equatorward edge of the auroral oval. The outer boundary of plasma in the equatorial plane, which maps to the poleward edge of the oval, is located in the distant magnetic tail where the processes are much more poorly understood. The second type of process is that which causes particles to precipitate: wave-particle interactions that result in pitch angle diffusion. Although particles may be able to populate field lines at high altitudes, they may not be observed in quantity at low altitudes if pitch angle diffusion is too weak. It is to better understand the processes governing particle motion in the magnetosphere that the auroral boundaries are studied for systematic variation.

For the 10 January example we have selected auroral boundaries from the electron and ion data and from the DMSP image along the sub-satellite track. Since the polar cap is well-defined by abrupt drops in particle intensity on the morning and evening sides of the oval and for both ions and electrons we choose both equatorward and poleward boundaries for examination. These are listed in Table 6 by the universal time of occurrence and the interpolated geographic latitude at 110 km. The evening equatorward electron boundary position picked at 56,904 is somewhat ambiguous due to the presence of a low intensity ramp in the electron flux. If the ramp is included in the boundary, it could be extended to 56,952 UT. All other boundaries are unambiguous. Both electron and ion precipitation have erratic low level fluxes on the equatorward morning edge. These may be due to a shrinking of the oval from a previous expanded state at high activity. The electron boundaries compare very well to those of the image with the exception of the morning equatorward boundary where the image boundary is higher by several degrees. For this case there is a ramp in morningside electron flux which is below the detection level of the imager. The ion boundaries compare less well with the image boundaries indicating that they produce a low level of light emission. The electron and ion boundaries have systematic differences. In general, the ion morning equatorward boundary is lower than the electron boundary. This trend is true for this pass if the electron evening boundary is taken at the sharp rise in integral flux. The ion and electron poleward boundaries are usually quite close. Here the evening poleward boundaries of the electrons and ions are identical.



Other typical features of aurora! precipitation are: (1) the morningside auroral oval is very broad and the smooth diffuse precipitation is rather distinctly separated from the discrete poleward features. The eveningside, by contrast, is narrow and the discrete electron structures collocate with the diffuse precipitation. (2) The eveningside ions are hotter than the morningside ions. The opposite is true for electrons: the morningside electrons are hotter than the eveningside.

Table 6. Electron and Ion Boundaries for 10 January 1983 Near 15 UT

Morning Equatorward Boundary			Morning Poleward Boundary		
	UT	GLAT		UT	GLAT
Electrons	55,944	56.1	Electrons	56,352	77.4
Ions	55,956	56.8	Ions	56,320	76.1
Image		62.5 $\pm$ 0.5	Image		77.3
Evening Equatorward Boundary			Evening Poleward Boundary		
Electrons	56,904(56,952)	64.8(62.1)	Electrons	56,808	69.9
Ions	56,940	62.8	Ions	56,808	69.9
Image		65.0 $\pm$ 0.5	Image		69.5

Radiation belt contamination was at times severe in the F2 and F4 detectors. High energy particles from the inner radiation belts penetrated the detector casing and stimulated the detector. This problem has been greatly reduced in the SSJ/4 detectors with increased shielding.

### 6.3 Discrete Arcs and Use of Electron Rejection Curves

In the following we present two examples of the use of the electron rejection curves to correct ion spectra. The examples were chosen to show both extreme and typical cases. The first examples are from the 10 January 1983 pass shown in Figure 18 and discussed above. Figure 18a shows that two morningside discrete arcs were observed between 56,195 sec and 56,290 sec UT. Both have inverted-V structure with individual spectra showing evidence of field aligned acceleration. In Figure 19 the integrated number flux above 1 keV and above 5 keV and the inferred field aligned potential,  $\phi_{||}$ , are plotted on an expanded scale for the time period spanning the observation of the arcs. One notes that there is a large increase in the greater than 5 keV integrated number flux at approximately 56,240 sec UT associated with a field aligned potential of  $\sim 6.5$  kV. In Figure 20 the measured and corrected electron and ion spectra at 56,241 sec UT within this enhancement

are shown. The measured and rejected count rates for the 20 ion channels are listed in Table 7 along with three other spectra to be discussed (the corrected counts are the measured minus the rejected counts). The table shows that the calculated counts due to electron scattering in this case are comparable to or greater than the measured counts for all of the low energy channels. Using the maximum rejection curve for the high energy channels reduces all counts to background or to the one count level. In Figure 21, the ion and electron spectra at 56,198 sec UT are plotted as in Figure 20. The electron spectrum is considerably softer than that in Figure 20. At this time, most of the precipitating electron flux was carried by electrons with energies below 5 keV. For such a case, the correction to the counts due to electron scattering is insignificant (see comparison of corrected and measured ion spectrum in Figure 21).

For the second example we chose a more extreme case of high energy electron precipitation found on 21 January 1983. A survey of the electron and ion data from 54,120 to 55,560 sec UT on that day is shown in Figure 22. The figure shows that there was a large increase in all three electron quantities near the poleward edge of the evening auroral zone indicating passage through a very intense electron acceleration region. Precipitating electron fluxes between 54,930 sec and 54,950 sec UT were generally an order of magnitude higher than the fluxes in the first examples. In Figures 23 and 24 we have plotted the electron and ion spectra at a time in the middle of the electron acceleration region and for a time near its edge respectively. The corrected and measured ion counts are again in Table 7. In the first set of spectra, at 54,938 sec UT, the electron scattering can account for all of the counts in the high energy ion channels and for most of the counts in the low energy ion channels. Because the spectrum is still rising at 30 keV these corrections are only a lower bound. The one channel with counts far exceeding any correction is channel 18 where counts exceeded 6000. This value is more than two orders of magnitude above the count level produced by electron scattering. The existence of such a high ion count confined to one or two channels of the low energy ion detector is a common feature of the data from within the electron acceleration region. The energy at which this ion peak is observed increases with increases in the level of the high energy electron flux. We interpret such peaks as indicating that the vehicle has charged to a negative potential due to the large current coming to the vehicle carried by the high energy electrons in the acceleration region. The ion peak results from ambient thermal ions being accelerated to the vehicle by the electric field associated with the negative potential. In Figure 24 the spectra at the edge of the acceleration region (UT ~ 54,919) are plotted for this case, as in the example shown in Figure 21. Since the electron flux has decreased the correction to the ion counts becomes small.

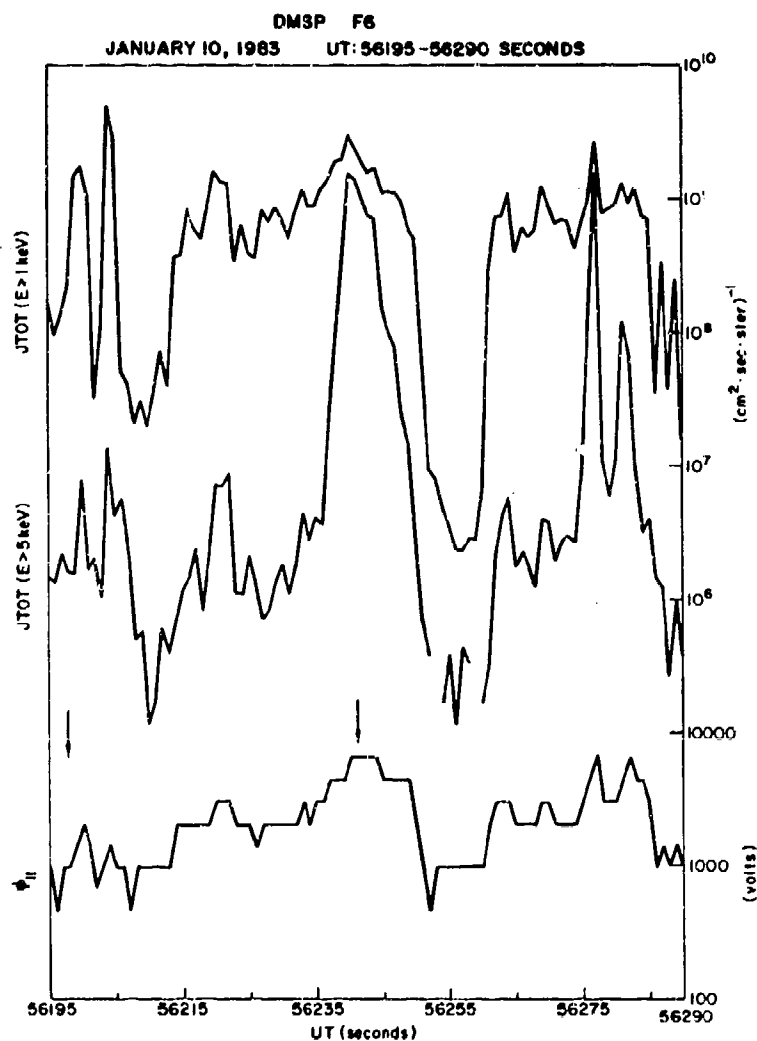


Figure 19. The Logarithm of the Integral Number Flux of Electrons Above 1 keV and 5 keV and the Logarithm of the Inferred Field Aligned Potential All Plotted for the Time Period Between 56,195 and 56,290 sec UT for a Pass of the F6 Satellite on 10 January 1983

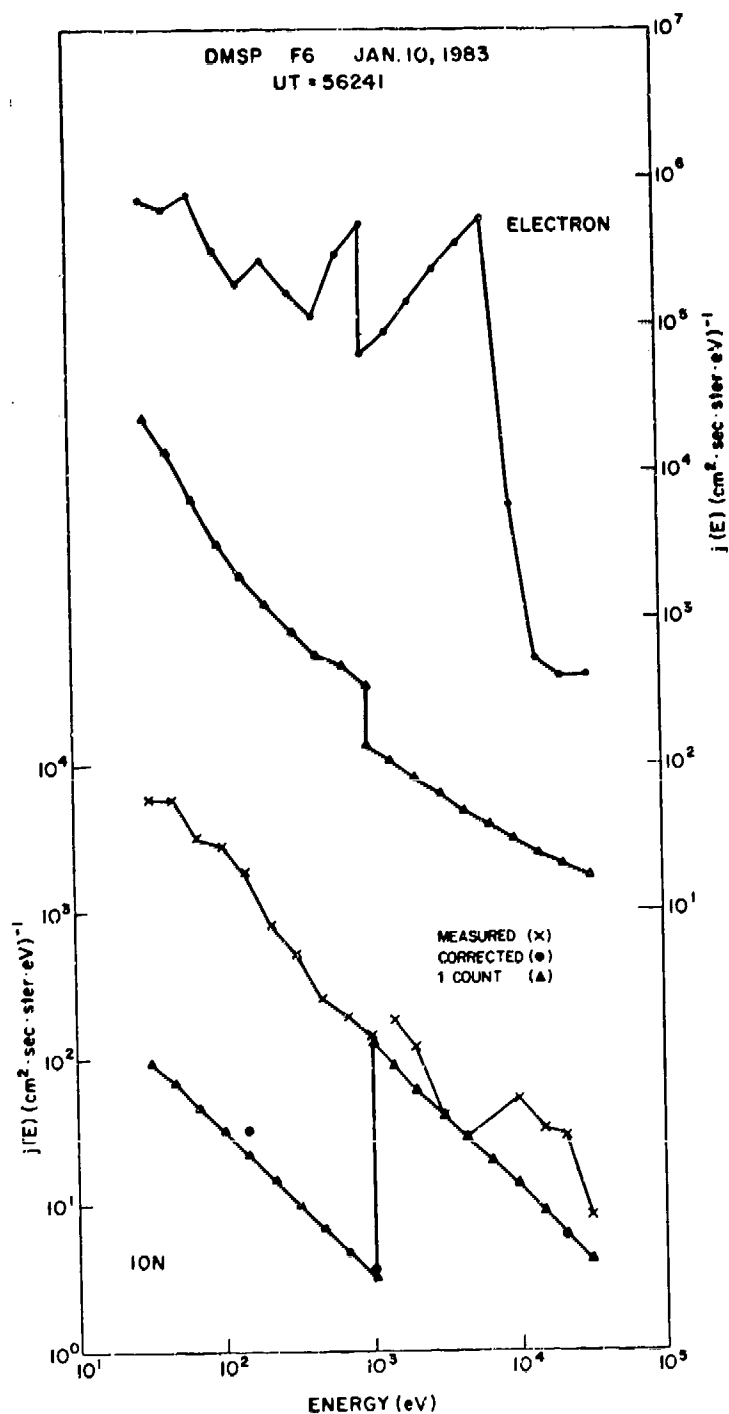


Figure 20. The Differential Number Flux Spectra for Electrons and Ions at 56,241 sec UT on 10 January 1983. The top spectrum is the measured electron spectrum; the second is the one count level for electrons. The bottom three are ion spectra: the initial spectrum and spectrum corrected for electron scattering through the analyzer and the one count level are shown. For the corrected ion spectrum only points where the corrected counts were greater than zero are plotted

Table 7. Measured and Corrected Ion Counts for Spectra on  
10 and 21 January 1983

Ch. No.	10 January				21 January			
	56,198		56,241		54,919		54,938	
	CR <sub>m</sub>	CR <sub>r</sub>	CR <sub>m</sub>	CR <sub>r</sub>	CR <sub>m</sub>	CR <sub>r</sub>	CR <sub>m</sub>	CR <sub>r</sub>
1	4	1	2	4	0	0	5	8
2	10	1	5	4	0	0	2	8
3	17	1	4	4	0	0	1	8
4	7	1	4	4	0	0	2	8
5	51	1	2	4	0	0	3	8
6	16	1	1	4	0	0	3	8
7	8	1	1	4	0	0	3	8
8	3	1	2	4	0	0	4	8
9	0	1	2	4	0	0	2	8
10	0	1	0	4	0	0	0	8
11	28	2	43	42	3	1	131	67
12	14	2	41	46	3	1	115	75
13	17	3	37	56	4	1	99	79
14	7	3	51	62	9	1	111	81
15	3	3	55	75	63	1	111	88
16	2	3	85	83	18	2	111	93
17	3	3	87	89	21	2	311	96
18	0	3	67	93	45	2	6623	99
19	2	3	85	96	15	2	143	100
20	3	3	61	98	22	2	123	101

m = measured

r = rejected

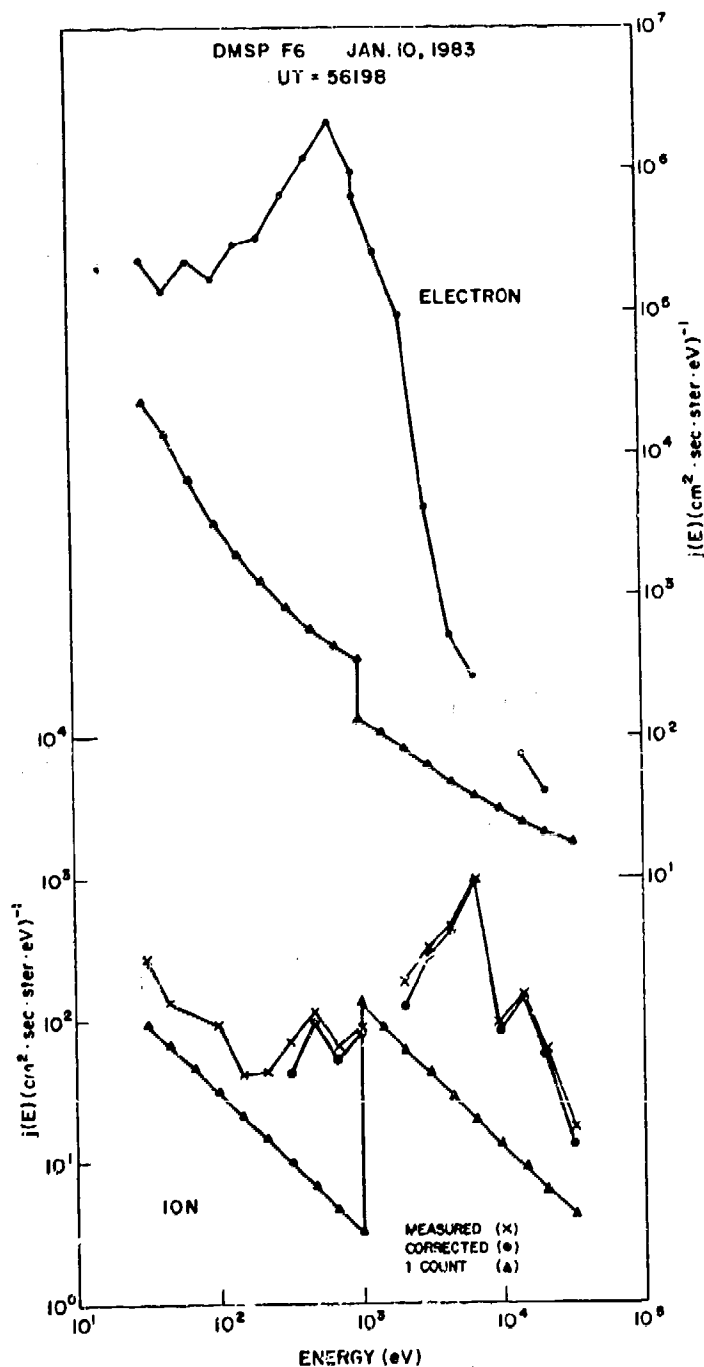


Figure 21. The Differential Number Flux Spectra for Electrons and Ions at 56,198 sec UT on 10 January 1983. The top spectrum is the measured electron spectrum; the second is the one count level for electrons. The bottom three are ion spectra: the initial spectrum and spectrum corrected for electron scattering through the analyzer and the one count level are shown. For the corrected ion spectrum only points where the corrected counts were greater than zero are plotted

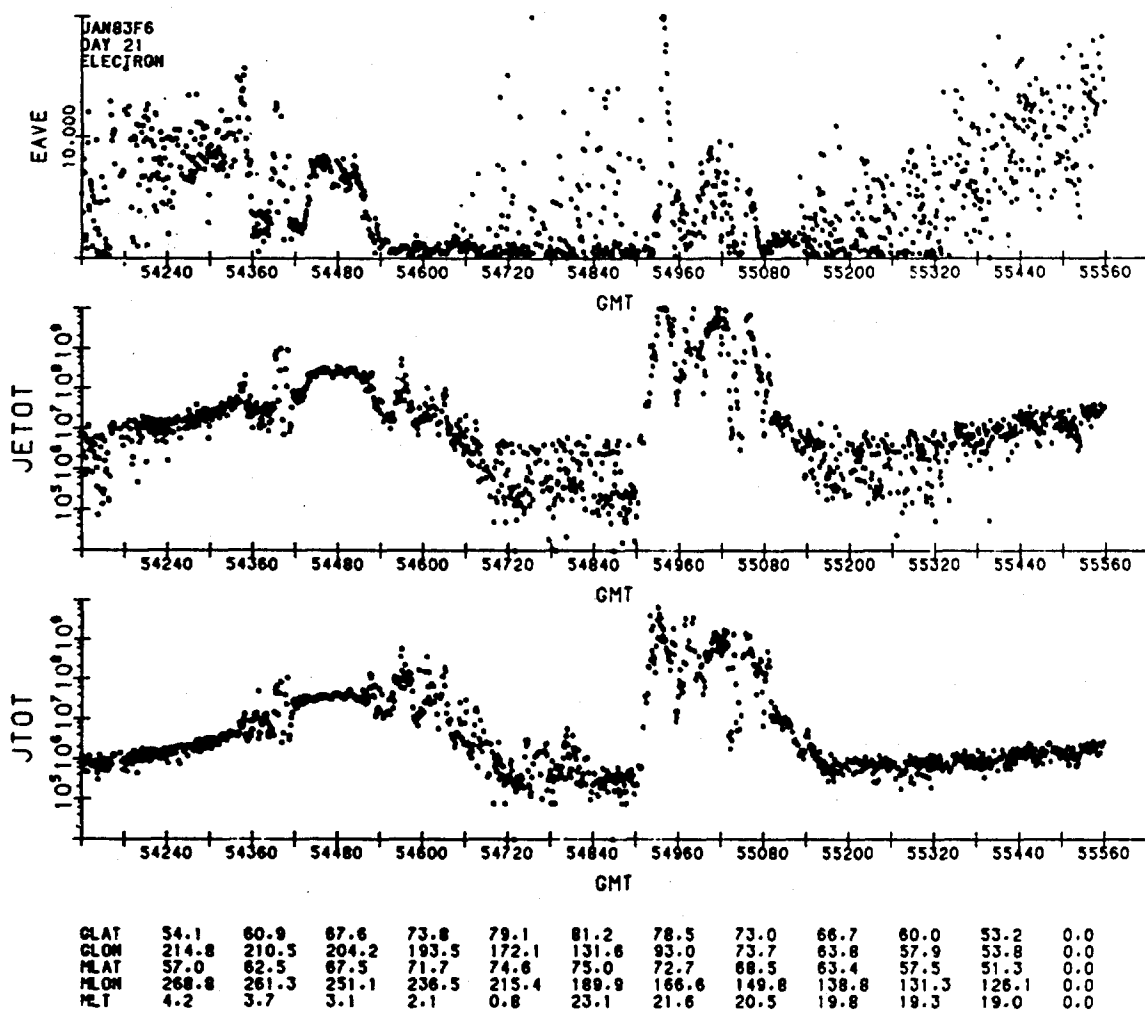


Figure 22a. Electron Data Plotted as in Figure 18 for a North Pole Pass of the F6 Satellite Between 15:02 UT (54,120 sec) and 15:27 UT (55,620 sec) on 21 January 1983

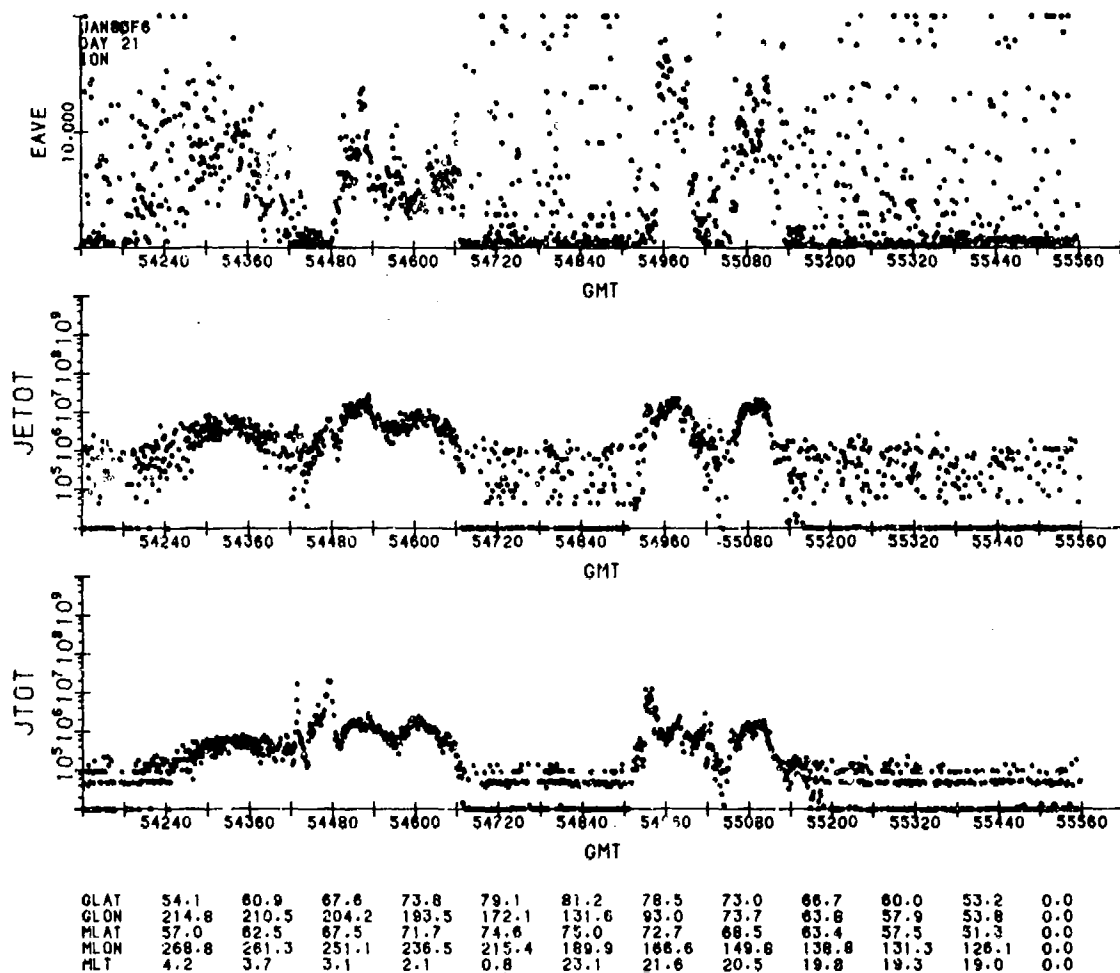


Figure 22b. Ion Data Plotted as in Figure 18 for a North Pole Pass of the F6 Satellite Between 15:02 UT (54,120 sec) and 15:27 UT (55,620 sec) on 21 January 1983



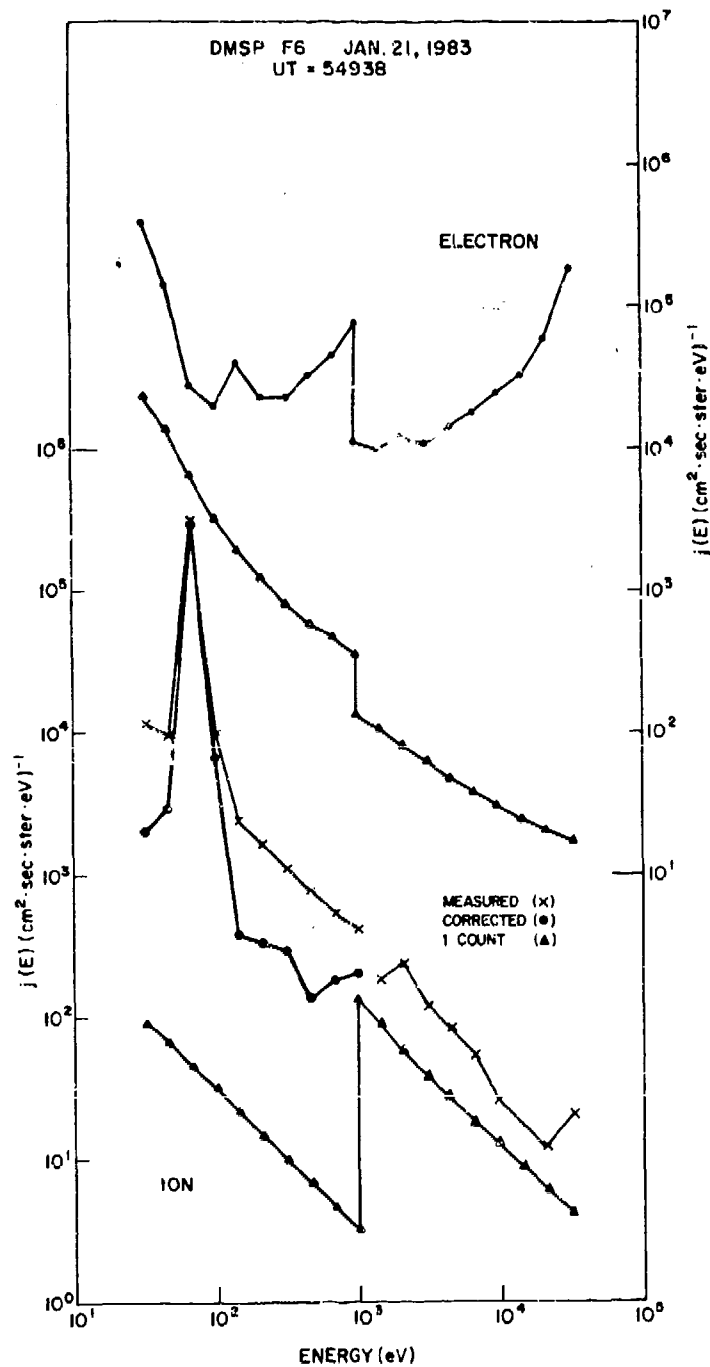


Figure 23. The Differential Number Flux Spectra for Electrons and Ions at 54,938 sec UT on 21 January 1983. The top spectrum is the measured electron spectrum; the second is the one count level for electrons. The bottom three are ion spectra: the initial spectrum and spectrum corrected for electron scattering through the analyzer and the one count level are shown. For the corrected ion spectrum only points where the corrected counts were greater than zero are plotted

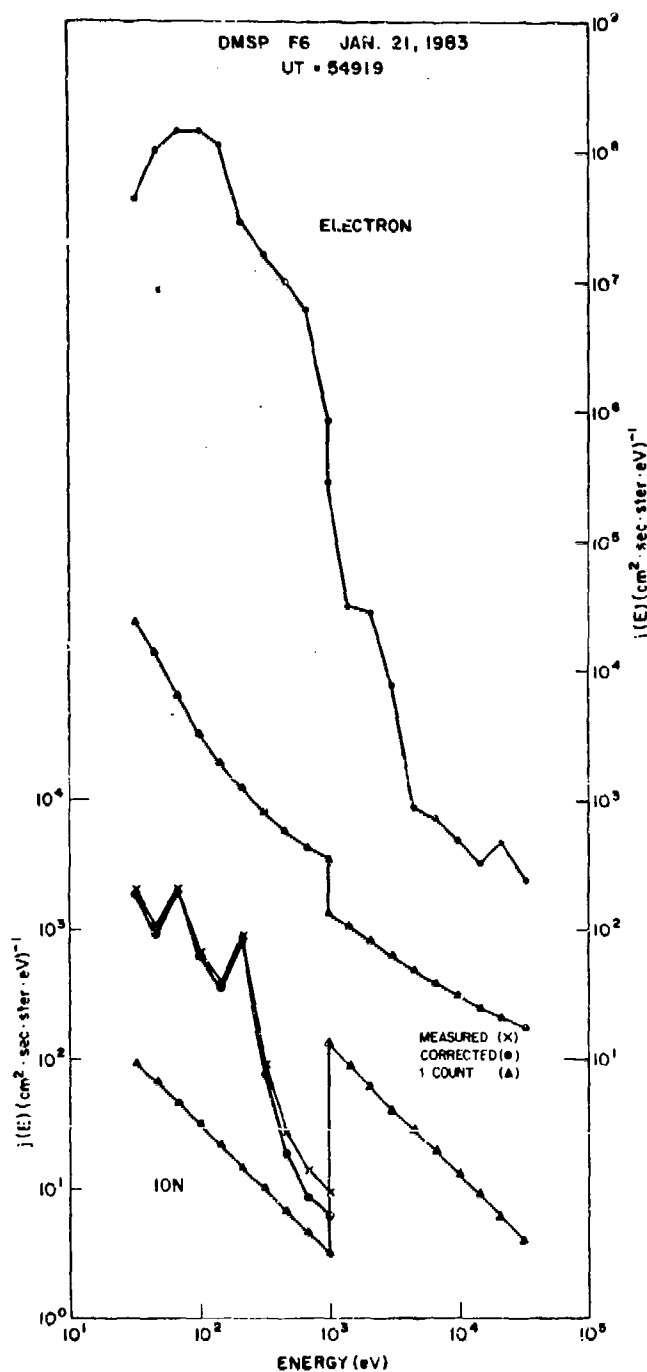


Figure 24. The Differential Number Flux Spectra for Electrons and Ions at 54,919 sec UT on 21 January 1983. The top spectrum is the measured electron spectrum; the second is the one count level for electrons. The bottom three are ion spectra: the initial spectrum and spectrum corrected for electron scattering through the analyzer and the one count level are shown. For the corrected ion spectrum only points where the corrected counts were greater than zero are plotted

#### 6.4 Ion Signatures in the Polar Rain

The large geometric factors in the SSJ/4 ion detector have made it possible to detect precipitating ion features in the polar cap. In this section we will discuss one of the ion signatures that we found in a study of the quiet cap to exemplify the use of ion data. The data were chosen from F6 passes occurring between 1 January 1983 and 5 July 1983 that satisfied the criterion that the precipitation profiles from both ions and electrons exhibit smooth and structureless low level fluxes. For electrons this precipitation is called the polar rain and has been studied extensively (see for example,<sup>7</sup> Gussenhoven et al). However, ion fluxes in the polar rain have until now remained undetected because of the low geometric factors of previous ion detectors. In all, 53 polar cap passes were analyzed. In each pass, the ion counts were summed over 300-sec intervals and time averaged distribution functions and differential spectra were calculated. Background noise in the low energy channels was identified by averaging the lowest counts in the 10 channels of the low energy sensor and subtracting this value from the counts in the remaining low energy channels.

The summed counts for polar cap ions for the 10 January 1983 pass discussed above are listed in Table 8. The counts peak in the lowest energy channels of the low energy detector head. The background in the low energy detector is 106 counts which is the average of the counts in channels 11 through 15. This averaged background count was subtracted from the counts in each low energy channel. All counts in the high energy detector are taken as background. The time averaged distribution function was calculated from the corrected counts and is shown in Figure 25. The spectrum is Maxwellian with a temperature of 20 eV and a density of  $6.3 \times 10^{-3} \text{ cm}^{-3}$ .

Table 8. Ion Count Rates for 10 January 1983; An Example of a Maxwellian Distribution

Channel No.	Energy (eV)	Ion Counts (Accumulated, 300 sec)
1	30,000	29
2	20,440	18
3	13,920	17
4	9480	32
5	6460	29
6	4400	20
7	3000	29
8	2040	22
9	1390	35
10	948	25
11	948	109
12	646	94
13	440	102
14	300	113
15	204	111
16	139	130
17	95	173
18	65	313
19	44	337
20	30	289

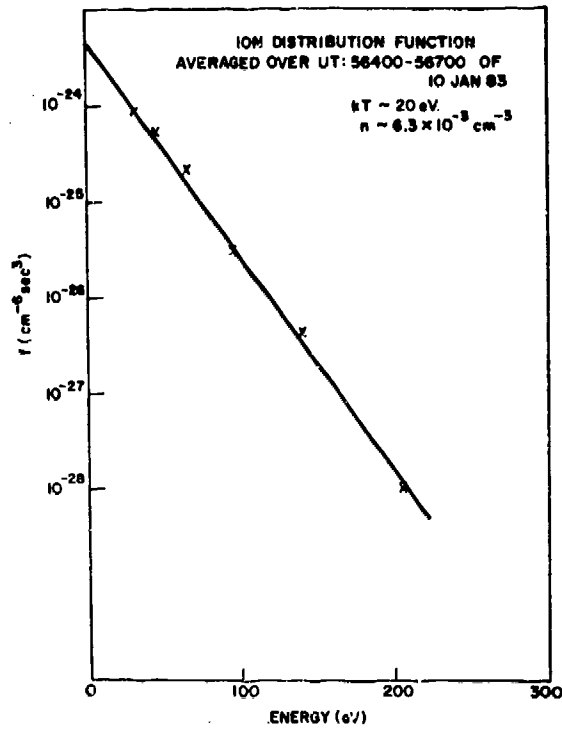


Figure 25. The Logarithm of the Measured Ion Distribution Function in the Polar Rain Plotted vs Energy on a Linear Scale. The straight line gives the linear least squares fit to the data. The values of  $kT$  and  $n$  are from this fit

## References

1. Hardy, D.A., Gussenhoven, M.S., and Huber, A. (1979) The Precipitating Electron Detectors (SSJ/3) for the Block 5D/Flights 2-5 DMSP Satellites: Calibration and Data Presentation, AFGL-TR-79-0210, AD A083136.
2. Gussenhoven, M.S., Hardy, D.A., and Burke, W.J. (1981) DMSP/F2 electron observations of equatorward auroral boundaries and their relationship to magnetospheric electric fields, J. of Geophys. Res., 86:768.
3. Gussenhoven, M.S. (1982) Extremely high latitude arcs, J. of Geophys. Res., 87:2401.
4. Hardy, D.A., Burke, W.J., Gussenhoven, M.S., Heinemann, N., and Holeman, E. (1981) DMSP/F2 electron observations of equatorward auroral boundaries and their relationship to the solar wind velocity and the north-south component of the interplanetary magnetic field, J. of Geophys. Res., 86:9961.
5. Hardy, D.A., and MacKean, R. (1980) An Algorithm for Determining the Boundary of Auroral Precipitation Using Data From the SSJ/3 Sensor, AFGL-TR-80-0028, AD A084482.
6. Hardy, D.A., Gussenhoven, M.S., and Holeman, E. (1984) Statistical model of auroral electron precipitation, submitted to J. of Geophys. Res.
7. Gussenhoven, M.S., Hardy, D.A., Heinemann, N., and Burkhardt, K. (1984) Morphology of the polar rain, J. of Geophys. Res., 89:9785.
8. Hardy, D.A., Burke, W.J., and Gussenhoven, M.S. (1982) DMSP optical and electron measurements in the vicinity of polar cap arcs, J. of Geophys. Res., 87:2413.
9. Hardy, D.A. (1984) Intense fluxes of low-energy electrons at geomagnetic latitudes above 85°, J. of Geophys. Res., 89:3883.
10. Gussenhoven, M.S., Hardy, D.A., Heinemann, N., and Holeman, E. (1982) Diffuse Auroral Boundaries and a Derived Auroral Boundary Index, Rep. AFGL-TR-82-0398, AD A130175.

## References

11. Gussenhoven, M.S., Hardy, D.A., and Heinemann, N. (1983) Systematics of the equatorward diffuse auroral boundary, J. of Geophys. Res., 88:5692.
12. Burke, W.J., Gussenhoven, M.S., Kelly, M.C., Hardy, D.A., and Rich, F.J. (1982) Electric and magnetic field characteristics of discrete arcs in the polar cap, J. of Geophys. Res., 87:2431.
13. Frank, L.A., Craven, J.D., Burch, J.L., and Winningham, J.D. (1982) Polar views of the earth's aurora with dynamics explorer, Geophysics Research Letters, 82:1001.
14. Smiddy, M., Sagalyn, R.C., Sullivan, W.P., Wildman, P.J.L., Anderson, P., and Rich, F. (1978) The Topside Ionosphere Plasma Monitor, (SSIE) for the Block 5D/Flight 2 DMSP Satellite, AFGL-TR-78-0071, AD A058503.
15. Marshall, F.J., Hardy, D.A., Huber, A., McGarity, J., Pantazis, J., and Winningham, D. (1984) A calibration system for electrostatic analyzers in the energy range (0 - 50 keV), manuscript in preparation for submission to Rev. of Sci. Instru.
- A1. Riehl, K., and Hardy, D.A. (1985) Average characteristics of polar rain electrons, to be submitted to J. Geophys. Res.

## Appendix A

### Anomalies in the F6 Electron Detector.

In analyzing the data from the low energy electron analyzer for the F6 satellite we have noted two problems. First, at all times, the counts observed in the three lowest energy channels are anomalously low. Second, the ratio of counts in channel 10 to channel 11 appears to increase as the counts in channel 10 increases. We attribute both of these effects to decreases in detection efficiency of the low energy electron analyzer. The first represents a decrease in efficiency with decreasing energy; the second a decrease in efficiency in all ten low energy electron channels with increasing flux. The reason for such effects are not known but we hypothesize that they may be the result of hydrocarbon contamination of the channel-trons. In order to know the real electron spectrum both effects must be corrected for in the conversion from counts to flux.

To correct for the effect in the three lowest energy channels 1-min averages of the count rate spectrum of the polar rain were calculated. For each 1-min average the count rates were converted to values of the distribution function. From previous work,<sup>A1</sup> we know that the low energy portion of the polar rain is generally Maxwellian in shape. This was confirmed in the new data where, except for a roll off in the three lowest energy channels, plots of the logarithm of the distribution function versus energy were approximately straight lines. To correct the three lowest channels the higher energy channels in such plots were linear least squares

---

A1. Riehl, K., and Hardy, D.A. (1985) Average characteristics of polar rain electrons, to be submitted to J. Geophys. Res.



fit to a straight line. The ratio between the value from the fit and value from the calculated distribution function was determined for each of the three lowest energy channels. Two hundred fifty two, 1-min segments of data were treated in this manner taken randomly from polar rain observations between 1 January and 5 July 1983. The average ratios were determined to be 1.17, 1.29, and 1.20 for channels 18, 19, and 20 respectively.

To correct for the second effect we selected 50 well-structured inverted-V regions. In the 50 events the counts in channel 10 covered a range from 0 to  $2.0 \times 10^4$ . For each electron spectrum in the 50 cases we calculated the ratio of the counts in channel 10 to channel 11. The values of the ratio were binned according to the counts in channel 10 used to calculate the ratio. The values from all 50 cases were then used to calculate the average ratio in each bin. Since the central energies of channel 10 and 11 are close, on average, the ratio for the counts in the two channels should be a constant, equal to the ratio of the two channels' energy independent geometric factors. In Figure A1 we see that the average ratio increases approximately linearly with the logarithm of the count level in channel 10. Such an increase implies a logarithmic decrease in the detection efficiency of channel 11 with count rate.

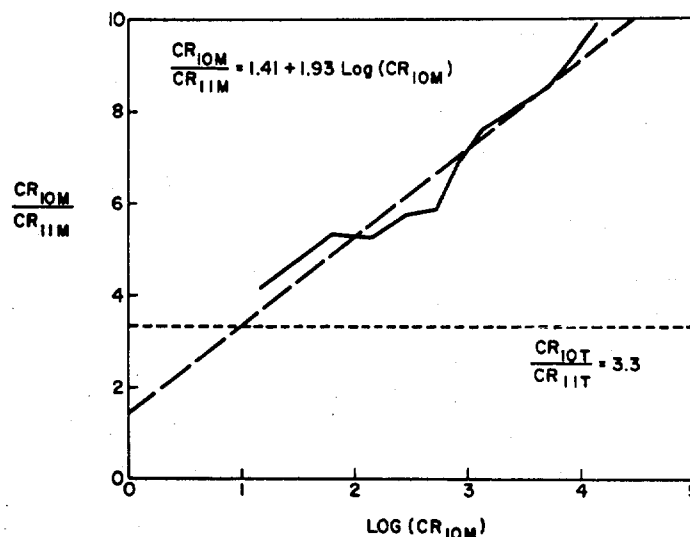


Figure A1. The Average Ratio of the Counts in Electron Channel 10 to the Counts in Electron Channel 11 Plotted vs the Logarithm of the Average Counts in Electron Channel 10. The horizontal dashed line gives the expected ratio if there is no decrease in efficiency with count rate. The second dashed line is the linear least squares fit to the measured ratio

The sloped dashed line in Figure A1 is the least squares fit to the ratio variation. The equation for the curve is

$$\frac{CR_{10M}}{CR_{11M}} = 1.41 + 1.93 \log(CR_{10M}), \quad (A1)$$

where the subscripts M refer to measured counts for the F6 detector. The horizontal dashed line gives the ratio based on the calibration geometric factors, that is,

$$\frac{CR_{10T}}{CR_{11T}} = 3.3, \quad (A2)$$

where the subscript T refers to values if there is no decrease in detector efficiency. We also know that

$$CR_{10T} = CR_{10M}. \quad (A3)$$

Substituting Eqs. (A2) and (A3) into Eq. (A1) we get

$$CR_{11M} = \frac{3.3 CR_{11T}}{1.41 + 1.93 \log(3.3 CR_{11T})}. \quad (A4)$$

For practical purposes we wish to find  $CR_{11T}$  as a function of  $CR_{11M}$ . Equation (A4) indicates that this function is nonlinear. If we calculate the ratio  $(CR_{11T}/CR_{11M})$  for a specific  $CR_{11M}$  using Eqs. (A1), (A2), and (A3) and plot that ratio vs the logarithm of  $CR_{11M}$  we get the curve as shown in Figure A2. This curve is well approximated by

$$\frac{CR_{11T}}{CR_{11M}} = 0.77 + 0.65 \log(CR_{11M}). \quad (A5)$$

Assuming that all the low energy channels behave similarly we get that

$$CR_{iT} = (0.77 + 0.65 \log CR_{iM}) CR_{iM}. \quad (A6)$$

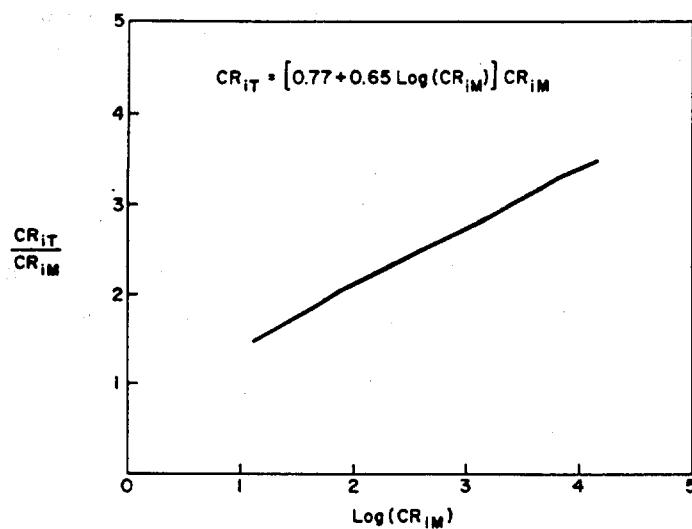


Figure A2. The Ratio of the True Counts to the Measured Counts for the Low Energy Electron Channels of the F6 SSJ/4 Detector Plotted vs the Logarithm of the Measured Counts

Thus for any  $CR_{iM}$  in any of the ten low energy channels Eq. (A6) will give the count rate adjusted for the loss in detection efficiency. For the three lowest energy channels the count rate additionally must be multiplied by the factors cited earlier.